

The MUSE-Wide Survey: A determination of the Lyman α emitter luminosity function at $3 < z < 6^{*,**}$

Edmund Christian Herenz¹, Lutz Wisotzki², Rikke Saust², Josephine Kerutt², Tanya Urrutia², Catrina Diener³, Kasper Borello Schmidt², Raffaella Anna Marino⁴, Geoffroy de la Vieuville⁵, Leindert Boogaard⁶, Joop Schaye⁶, Bruno Guiderdoni⁷, Johan Richard⁷, and Roland Bacon⁷

¹ Department of Astronomy, Stockholm University, AlbaNova University Centre, 106 91 Stockholm, Sweden
e-mail: christian.herenz@astro.su.se

² Leibniz-Institut für Astrophysik Potsdam (AIP), An der Sternware 16, 14482 Potsdam, Germany

³ University of Cambridge, Madingley Road, Cambridge CB3 0HA, UK

⁴ ETH Zürich, Department of Physics, Wolfgang-Pauli-Strasse 27, 8093 Zürich, Switzerland

⁵ Institut de Recherche en Astrophysique et Planétologie (IRAP), Université de Toulouse, CNRS, UP, CNES, 14 Avenue Edouard Belin, 31400 Toulouse, France

⁶ Leiden Observatory, Leiden University, PO Box 9513, 2300 RA Leiden, The Netherlands

⁷ Univ. Lyon, Univ. Lyon1, ENS de Lyon, CNRS, Centre de Recherche Astrophysique de Lyon UMR5574, 69230 Saint-Genis-Laval, France

Received 30 August 2018 / Accepted 2 November 2018

ABSTRACT

We investigate the Lyman α emitter (LAE) luminosity function (LF) within the redshift range $2.9 \leq z \leq 6$ from the first instalment of the blind integral field spectroscopic MUSE-Wide survey. This initial part of the survey probes a region of 22.2 arcmin^2 in the CANDELS/GOODS-S field (24 MUSE pointings with 1h integrations). The dataset provided us with 237 LAEs from which we construct the LAE LF in the luminosity range $42.2 \leq \log L_{\text{Ly}\alpha} [\text{erg s}^{-1}] \leq 43.5$ within a volume of $2.3 \times 10^5 \text{ Mpc}^3$. For the LF construction we utilise three different non-parametric estimators: the classical $1/V_{\text{max}}$ method, the C^- method, and an improved binned estimator for the differential LF. All three methods deliver consistent results, with the cumulative LAE LF being $\Phi(\log L_{\text{Ly}\alpha} [\text{erg s}^{-1}] = 43.5) \approx 3 \times 10^{-6} \text{ Mpc}^{-3}$ and $\Phi(\log L_{\text{Ly}\alpha} [\text{erg s}^{-1}] = 42.2) \approx 2 \times 10^{-3} \text{ Mpc}^{-3}$ towards the bright and faint end of our survey, respectively. By employing a non-parametric statistical test, and by comparing the full sample to subsamples in redshift bins, we find no supporting evidence for an evolving LAE LF over the probed redshift and luminosity range. Using a parametric maximum-likelihood technique we determine the best-fitting Schechter function parameters $\alpha = -1.84^{+0.42}_{-0.41}$ and $\log L^* [\text{erg s}^{-1}] = 42.2^{+0.22}_{-0.16}$ with the corresponding normalisation $\log \phi^* [\text{Mpc}^{-3}] = -2.71$. However, the dynamic range in Ly α luminosities probed by MUSE-Wide leads to a strong degeneracy between α and L^* . Moreover, we find that a power-law parameterisation of the LF appears to be less consistent with the data compared to the Schechter function, even so when not excluding the X-Ray identified AGN from the sample. When correcting for completeness in the LAE LF determinations, we take into account that LAEs exhibit diffuse extended low surface brightness halos. We compare the resulting LF to one obtained by applying a correction assuming compact point-like emission. We find that the standard correction underestimates the LAE LF at the faint end of our survey by a factor of 2.5. Contrasting our results to the literature we find that at $\log L_{\text{Ly}\alpha} [\text{erg s}^{-1}] \lesssim 42.5$ previous LAE LF determinations from narrow-band surveys appear to be affected by a similar bias.

Key words. cosmology: observations – galaxies: high-redshift – galaxies: luminosity function, mass function – techniques: imaging spectroscopy

1. Introduction

One of the most fundamental statistical distribution functions to characterise the population of galaxies is the galaxy luminosity function (LF). The differential LF, $\psi(L, z)$, counts the number of galaxies N per unit volume V as a function of luminosity L and redshift z : $dN = \psi(L, z) dL dV dz$. While this

bi-modal form provides the most general description, observationally the LF is often determined at a fixed redshift or a redshift interval over which effects of redshift evolution are deemed negligible, i.e.

$$dN = \phi(L) dL dV. \quad (1)$$

Galaxy LFs and their redshift evolution provide a gold standard for summarising the changing demographics of galaxies with cosmic look-back time. Being essential benchmarks for cosmological models of galaxy formation and evolution in our universe, LF determinations are often amongst the pivotal goals in the design and analysis of extragalactic surveys (Petrosian 1992; Willmer 1997; Johnston 2011; Dunlop 2013; Caditz 2016).

While Lyman α (Ly α , $\lambda 1216$) emission was already suggested as a prime tracer for galaxy formation studies in the early

* Based on observations collected at the European Organisation for Astronomical Research in the Southern Hemisphere under ESO programme 094.A-025.

** The Lyman α emitter catalogue, the Lyman α emitter selection functions, as well as the likelihood function and its normalisation for a Schechter parametrisation are only available at the CDS via anonymous ftp to cdsarc.u-strasbg.fr (130.79.128.5) or via <http://cdsarc.u-strasbg.fr/viz-bin/qcat?J/A+A/621/A107>

universe more than five decades ago (Partridge & Peebles 1967), initial searches for such high- z Ly α emitting galaxies (LAEs) were unsuccessful and, hence, constrained only upper limits of the LAE LF (see review by Pritchett 1994).

The first successful detections of LAEs accompanied by spectroscopic confirmations on 8 m class telescopes employed a colour-excess criterion in narrow-band (NB) images (Hu & McMahon 1996; Hu et al. 1998). In the following years the NB imaging technique was routinely used to construct LAE samples of up to several hundreds of galaxies at $2 \lesssim z \lesssim 5$ (see review by Taniguchi et al. 2003). Mostly from such NB surveys, sometimes in combination with spectroscopic follow-up of subsamples, the first LAE LF estimates up to $z \sim 6$ were obtained (e.g. Cowie & Hu 1998; Kudritzki et al. 2000; Ouchi et al. 2003; Hu et al. 2004; Ajiki et al. 2004; Tapken et al. 2006; Dawson et al. 2007; Gronwall et al. 2007; Murayama et al. 2007; Sawicki et al. 2008; Henry et al. 2012).

Most of the LAE LF studies so far focused on a single redshift slice of typically $\Delta z \approx 0.1$ (corresponding to typical NB filter widths $\Delta\lambda \approx 100 \text{ \AA}$). Significant progress in terms of methodology, numbers of LAEs, and rate of spectroscopic follow-up observations was achieved by Ouchi et al. (2008) within three redshift slices ($z \sim \{3, 4, 5\}$) over a 1 deg^2 region in the *Subaru/XMM-Newton* Deep Survey (SXDS; Furusawa et al. 2008). Later, Ouchi et al. (2010) extended the SXDS LAE survey to $z \approx 6.6$. More recently, further *Subaru/Suprime-Cam* NB imaging data in other fields were used to construct LAE LFs over 5 deg^2 at $z = 5.7$ and $z = 6.6$ (Matthee et al. 2015; Santos et al. 2016). Moreover, by combining NB and medium-band observations from the Subaru and the *Isaac Newton* Telescope Sobral et al. (2018a) constructed a LAE LF from ~ 4000 LAEs simultaneously from redshifts $z \sim 2$ to $z \sim 6$.

The latest development in NB LAE surveys is due to the advent of *Subaru/Hyper Suprime-Cam*, a 1.5 deg^2 wide-field imager (Miyazaki et al. 2012, 2018). Recently, the first results for a $\sim 14 \text{ deg}^2$ and $\sim 21 \text{ deg}^2$ NB survey at $z \sim 6$ and $z \sim 7$, respectively, were published (the so called SILVERUSH survey Ouchi et al. 2018; Shibuya et al. 2018a,b). From this unprecedented dataset Konno et al. (2018) constructed the LAE LF for sources $L_{\text{Ly}\alpha} \gtrsim 10^{43} \text{ erg s}^{-1}$. Without any doubt NB imaging studies have been and are still of central importance for our understanding of the LAE LF. Only their wide nature allows the construction of statistical samples of the brightest and rarest LAEs.

However, the LAE LF determination from NB imaging studies is fraught with some difficulties that can be alleviated in blind surveys with an integral field spectrograph (IFS, see e.g. the recent textbook by Bacon & Monnet 2017). Especially, since an IFS samples spectra over a contiguous field of view, the resulting 3D datacubes can be envisioned as a stack of NB images of much smaller bandwidth compared to imaging NB filters. Thus, a blind search for emission line sources in an IFS datacube directly provides a catalogue of spectroscopically confirmed Ly α emitters, avoiding the need for follow-up spectroscopy. Then, flux measurements on the lines can be performed in virtually any conceivable aperture, resulting in reliable flux measurements absent of slit or bandpass losses. Moreover, instead of probing only a tiny redshift slice, IFSs cover an extended range of redshifts. Another advantage is that the narrow bandwidth of the individual wavelength slices in the datacube significantly reduces the contribution of sky background to emission line signals. This allows IFS searches to reach significant fainter limiting fluxes compared to NB imaging surveys. Lastly, by construction an integral field spectroscopic survey delivers a flux-limited LAE sample, rather

than an equivalent-width limited sample. This mitigates possible biases from heterogeneous equivalent width cuts in NB imaging studies.

A pilot IFS survey for LAEs between $3 < z < 6$ was performed by van Breukelen et al. (2005) with the Visible Multi Object Spectrograph (Le Fèvre et al. 2003) Integral Field Unit at ESOs Very Large Telescope (VLT). However, this pilot study was severely limited by the relatively low throughput, small field of view, and the low spectral resolution of this instrument. Substantial progress in performing a blind IFS survey to detect Ly α emitters was achieved in the Hobby Eberle Telescope Dark Energy Experiment (HETDEX) Pilot Survey by Adams et al. (2011). Utilising 61 nights of observations with VIRUS-P (Hill et al. 2008), a path-finder fibre-fed IFS that will be replicated 156 times for the final HETDEX survey (Hill & HETDEX Consortium 2016) on the McDonald 2.7 m Harlan J. Smith telescope, Adams et al. (2011) constructed a catalogue of 397 emission line galaxies blindly selected over 169 arcmin^2 in areas with rich complementary datasets. This catalogue contained 99 LAEs without X-ray counterparts in the range $1.9 < z < 3.8$. From the Adams et al. (2011) catalogue Blanc et al. (2011) constructed the Ly α LF in the luminosity range $42.6 \leq \log L_{\text{Ly}\alpha} [\text{erg s}^{-1}] \leq 43.5$.

With the advent of the Multi Unit Spectroscopic Explorer (MUSE) at ESOs VLT (Bacon et al. 2014; Caillier et al. 2014) the field of blind deep IFS surveys was revolutionised. This image-slicer-based IFS with a $1' \times 1'$ field of view covering the wavelength range from 4650 \AA to 9300 \AA was designed from the ground up as a discovery machine for faint emission line galaxies, especially LAEs at high redshift ($2.9 \lesssim z \lesssim 6.6$, Bacon et al. 2004).

Its unprecedented potential for LAE LF determinations was demonstrated in the analysis of a 27 h integration on the *Hubble* Deep Field South (Casertano et al. 2000) obtained during commissioning (Bacon et al. 2015). By utilising 59 LAEs from this dataset Drake et al. (2017a) was able to put constraints on the Ly α LF down to $\log L_{\text{Ly}\alpha} [\text{erg s}^{-1}] = 41.4$, almost an order of magnitude deeper than nearly all previous observational efforts; the only exception was a heroic 92 h deep long-slit integration with the FORS2 instrument on ESOs VLT (Rauch et al. 2008). Recently, the Drake et al. (2017a) pilot-study was significantly refined by Drake et al. (2017b) using 601 LAEs found in the MUSE Consortium Guaranteed Time Observations (GTO, Bacon et al. 2017; Inami et al. 2017) of the *Hubble* Ultra Deep Field (Beckwith et al. 2006). This dataset consists of a $3.15' \times 3.15'$ mosaic exposed at 10h depth, and a central 1.15 arcmin^2 31h deep pointing that reached depths similar to those of the pilot study in the *Hubble* Deep field South. As a novelty Drake et al. (2017b) accounted for the effect of extended low surface brightness Ly α halos in their completeness assessment.

However, the pencil beam nature of the MUSE-deep fields does not allow us to probe the LAE LF at brighter luminosities. Thus, complementary to the MUSE Deep Fields a shallower large-area programme, known as MUSE-Wide (MW), is also part of the MUSE GTO. MUSE-Wide covers 100 arcmin^2 at 1h depth in regions where deep HST imaging surveys were performed, namely the CANDELS/Deep region in the *Chandra* Deep Field South (CDFs Grogin et al. 2011; Koekemoer et al. 2011) and the GOODS/South survey (Giavalisco et al. 2004). Recently, Herenz et al. (2017; hereafter H017) presented a catalogue of 831 emission line selected galaxies from the first 24 MUSE-Wide pointings (corresponding to an area of 22.2 arcmin^2) in the CDFS. This catalogue contains 237 LAEs

with luminosities $41.6 \leq \log L_{\text{Ly}\alpha} [\text{erg s}^{-1}] \leq 43.5$ in the redshift range $3 < z < 6$, thus augmenting the sample of faint LAEs from the MUSE-Deep fields. In the present manuscript we use the LAE sample obtained in the first 24 MUSE-Wide pointings to study the LAE LF.

The structure of this manuscript is as follows. In Sect. 2 we provide an overview of the MUSE-Wide survey data used and we describe how we obtained the LAE initial sample from this dataset. Following, in Sect. 3 we explain how we constructed the LAE selection function in MW. Then, in Sect. 4 we provide an overview of the methods adopted for constructing the LAE LF. Our results on the LAE LF are given in Sect. 5. In Sect. 6 we compare our results with those from the literature. Finally, we summarise the results obtained so far in Sect. 7, where we also present an outlook for further refinements of our study that will be relevant with the release of the full MUSE-Wide sample.

Throughout the paper we always assume a standard Λ CDM concordance cosmology with $\Omega_{\Lambda} = 0.7$, $\Omega_M = 0.3$, and $H_0 = 70 \text{ km s}^{-1}$ when converting observed to physical quantities.

2. MUSE-Wide data and Ly α emitter sample

The data under scrutiny in this paper are the 24 adjacent $1' \times 1'$ one-hour deep MUSE pointings in the CANDELS/Deep region of the GOODS-South field. The data were taken during the first period of MUSE GTO Observations between September and October 2014 (ESO programme ID 094.A-0205) as part of the MUSE-Wide (hereafter MW) survey. Accounting for the $4''$ overlap between individual pointings, the total survey area is 22.2 arcmin^2 . The survey covers a wavelength range from 4750 \AA to 9350 \AA , thus probing Ly α emitters within the redshift range $2.9 \leq z \leq 6.7$.

A detailed account of the observations, data reduction, and construction of the emission line selected galaxy catalogue has been given in H017; here we only provide an overview.

2.1. Observations and data reduction

Each 1h deep MW pointing consists of four individual 15-minute exposures. More than half of the observations were taken under photometric conditions during dark and grey nights, with the remainder taken under clear conditions during dark nights. The measured seeing ranged from $0.7''$ to $1.1''$, with $0.9''$ being the average of the observations.

For each of the pointings a datacube was created by employing the MUSE data reduction system (Weilbacher et al. 2014) in combination with a few custom developed routines and the Zurich Atmosphere Purge (ZAP) sky-subtraction software¹ (Soto et al. 2016a). We also used the self-calibration procedure that is part of the MUSE Python Data Analysis Framework – MPDAF² (Conseil et al. 2016; Bacon et al. 2017).

The reduced data consists of 24 datacubes, each covering $1' \times 1'$ on the sky with a spatial sampling $0.2'' \times 0.2''$. These spatial sampling elements (so-called spaxels) contain a spectrum from 4750 \AA – 9350 \AA that is sampled at 1.25 \AA in air wavelengths. Each volume element (called a voxel) of a datacube stores the received flux density in units of $10^{-20} \text{ erg s}^{-1} \text{ cm}^{-2} \text{ \AA}^{-1}$. The full width at half maximum (FWHM) of the spectrographs line spread function is roughly twice the spectral sampling (i.e.

$\sim 2.5 \text{ \AA}$) resulting in a resolving power of $R \sim 1900\text{--}3800$ over the wavelength range covered.

The MUSE data reduction system also propagates the variances during all reduction steps into each voxel, thereby creating a complementary variance datacube for each pointing. However, these formal variance values underestimate the true variances, and are thus not optimal for emission line detection and estimation of the error on emission line flux measurements. In order to correct for this, we performed an empirical estimate of the variance values by evaluating the statistics of randomly placed apertures in empty regions of the sky (see Sect. 3.1.1 in H017).

2.2. Emission line galaxy catalogue

Emission line source detection in the MW data is performed with our dedicated Line Source Detection and Cataloguing Tool LSDCat³ (Herenz & Wisotzki 2017). As a required preparatory step before emission line source detection we remove source continua from the datacube by subtracting a $\approx 190 \text{ \AA}$ wide running median in the spectral direction. This method of removing source continua has proven to be very effective, leaving as remaining features mostly real emission lines and straightforward identifiable residuals from continua that vary at higher frequencies than the width of the median filter (e.g. cold stars).

In the next step LSDCat cross-correlates each datacube with a 3D matched filter template for compact emission line sources. We used a 3D Gaussian as the template, with its spatial FWHM dictated by the wavelength dependent seeing point spread function (PSF) and its spectral FWHM fixed to $v_{\text{FWHM}} = 250 \text{ km s}^{-1}$. As demonstrated in Sect. 4.3 of Herenz & Wisotzki (2017), this value is optimal for detecting LAEs in MUSE surveys at their highest possible signal-to-noise ratios (S/N). Then the initial emission line candidate catalogue was created by setting the detection threshold to $S/N_{\text{thresh}} = 8$. This initial catalogue was then screened by four investigators (ECH, LW, TU, and JK) using the interactive graphical tool QtClassify⁴ (Kerutt 2017; see also Appendix of H017). The purpose of this screening process was to identify the detected emission lines, and to purge obviously spurious detections (e.g. those due to continuum residuals). Real detections were assigned with quality and confidence flags. Here, the quality flag encodes whether multiple emission lines of a source were detected (quality A), multiple emission lines are present but below the detection threshold (quality B), or whether the identification was based on a single line (quality C). By this definition all of the LAEs considered in the present analysis are quality C objects. As detailed in H017 (Sect. 3.1.4), the confidence values encode a more subjective measure of belief towards the final identification of a source, ranging from 1 (minor doubts) to 3 (no doubts). These values were assigned based on the apparent shape of the spectral profile and, if present, on the morphology and size of an optical counterpart in the HST images.

2.3. Lyman α emitter sample

The final emission line catalogue published in H017 consists of 831 emission line galaxies, with 237 Ly α emitting galaxies in the redshift range $2.97 \leq z \leq 5.99$. Two of these high- z galaxies

¹ ZAP is publicly available via the Astrophysics Source Code Library: <http://ascl.net/1602.003> (Soto et al. 2016b).

² MPDAF is publicly available via the Astrophysics Source Code Library: <http://ascl.net/1611.003> (Piqueras et al. 2017).

³ LSDCat is publicly available via the Astrophysics Source Code Library: <http://ascl.net/1612.002> (Herenz & Wisotzki 2016).

⁴ QtClassify is publicly available via the Astrophysics Source Code Library: <http://ascl.net/1703.011> (Kerutt 2017).

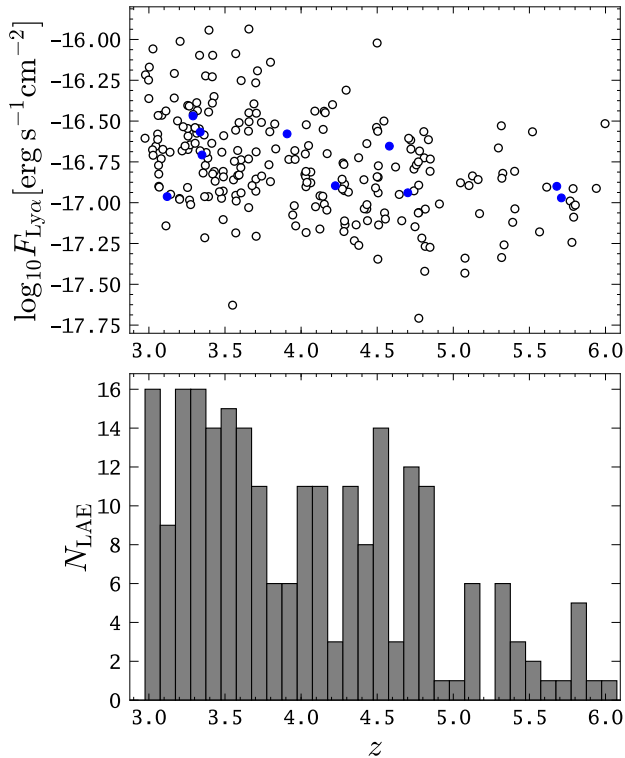


Fig. 1. *Top panel:* fluxes and redshifts of the MW LAE sample used in this study (open circles) in comparison to the fluxes and redshifts of the MUSE HDFS LAEs used to determine a realistic selection function as described in Sect. 3.2 (filled circles). *Bottom panel:* redshift histogram of the MW LAE sample (binning: $\Delta z = 0.1$).

exhibit clear signatures of active nuclei⁵ and are also flagged as active galaxies in the *Chandra* 7Ms source catalogue (Luo et al. 2017). Another object was classified as a strong C iv emitter, and is therefore also likely not a star-forming LAE⁶. We note that these AGN are also the most luminous LAEs in our sample. In our analysis below we discuss the effect of not excluding these bona fide AGNs when determining the LAE LF.

All except five of the 234 non-AGN LAE galaxies have only a single line detected by LSDCat. The five exceptions are characterised by strongly pronounced double-peaked Ly α profiles, with both peaks having individual entries in the emission line catalogue⁷. Moreover, only 20 sources have confidence value 1 assigned, i.e. there were minor doubts regarding their classification as Ly α . However, we found that excluding those low-confidence sources from our analysis had no impact on the resulting LF determinations.

Lyman α emitter redshifts were determined by fitting the spectral profiles. As detailed in H017 we used the fitting formula

$$f(\lambda) = A \times \exp\left(-\frac{(\lambda - \lambda_0)^2}{2 \times (a_{\text{asym}}(\lambda - \lambda_0) + d)^2}\right) \quad (2)$$

introduced by Shibuya et al. (2014) to adequately model the asymmetric spectral profiles of LAEs. The free parameters A , λ_0 , a_{asym} , and d in Eq. (2) are the amplitude, the peak wavelength, the asymmetry parameter, and the typical width of the line, respectively.

⁵ MW IDs 104014050 and 115003085.

⁶ MW ID 121033078.

⁷ MW IDs 106014046, 115005089, 110003005, 122021111, and 123018120.

Emission line fluxes F_{line} of the LAEs were determined with the automated flux extraction routine of LSDCat. In Herenz & Wisotzki (2017) we found that for LAEs in the MW survey the automatic measurements from the software compare best to a manual curve-of-growth analysis over the spectral and spatial extent of the emitters when aperture radii of three times the Kron-radius (Kron 1980) were used. Thus, we use these $F_{\text{line}}(3 \times R_{\text{Kron}})$ fluxes as the basis for our luminosity function analysis. The mean and median $3 \times R_{\text{Kron}}$ radii in which fluxes were extracted are 2.1'' and 2.0'', respectively, with values ranging from 1.8'' to 3.7''. However, we cautioned in H017 that quite frequently the spectral window of the automated flux extraction did not completely encompass the whole spectral profile of the LAEs. These profiles are often characterised by a weak secondary bump bluewards of the main spectral peak. This may result in flux losses. In order to correct for these losses, we first visually inspected all spectral profiles to classify them as single- or double-peaked. We found that 90 LAEs in our sample show a weaker secondary blue peak. We then fitted all double-peaked profiles with a linear combination of two profiles described by Eq. (2). From these fits we calculated the fraction of the line flux outside the spectral extraction window as flux correction factor. The average (median) flux correction factor for the double-peaked emitters derived from this procedure is 1.17 (1.16). Using the single component fits of Eq. (2) we also derived flux correction factors for the single-peaked LAE profiles. Here the correction factors are significantly smaller (mean: 1.03, median: 1.02), thus indicating the overall robustness of the automated procedure for simple emission line profiles. The final LAE fluxes used in our analysis are then obtained by multiplying the catalogued $F_{\text{line}}(3 \times R_{\text{Kron}})$ fluxes by each individually determined correction factor⁸. An overview of the fluxes and redshifts and a redshift histogram of the MW LAE sample are shown in Fig. 1.

Finally, the measured fluxes are converted into Ly α luminosities,

$$L_{\text{Ly}\alpha} = 4\pi F_{\text{Ly}\alpha} D_L^2(z), \quad (3)$$

where $D_L(z)$ is the luminosity distance corresponding to the redshift of the Ly α emitter that was determined from fitting the spectral line profile with Eq. (2).

3. MUSE-Wide Lyman α emitter selection function

To derive the luminosity function from the MW LAE sample, we first need to determine the selection function for LAEs in our integral-field spectroscopic survey. The selection function encodes the probability $f_C(F_{\text{Ly}\alpha}, \lambda)$ of observing a LAE with flux $F_{\text{Ly}\alpha}$ at wavelength λ in our survey. Given an adopted cosmology it can also be uniquely represented in redshift-luminosity space: $f_C(F_{\text{Ly}\alpha}, \lambda) \leftrightarrow f_C(L_{\text{Ly}\alpha}, z_{\text{Ly}\alpha})$.

In order to construct $f_C(F_{\text{Ly}\alpha}, \lambda)$ for MW, we studied the success rate of recovering artificially implanted LAEs with our detection procedure. In Sect. 3.1 we discuss this experiment as performed with model sources characterised by a compact point-like spatial profile and a simple spectral profile. Then, in Sect. 3.2, we discuss the experiment as performed under more realistic assumptions by accounting for the observed variety in spectral- and spatial profiles of LAEs. To this end we make use of real LAEs observed in the MUSE HDFS (Bacon et al. 2015). Finally, we explain in Sect. 3.3 how the measured recovery fractions are converted to selection functions $f_C(F_{\text{Ly}\alpha}, \lambda)$.

⁸ The catalogue of the LAE sample used in this publication is available as an associated data product via the CDS.

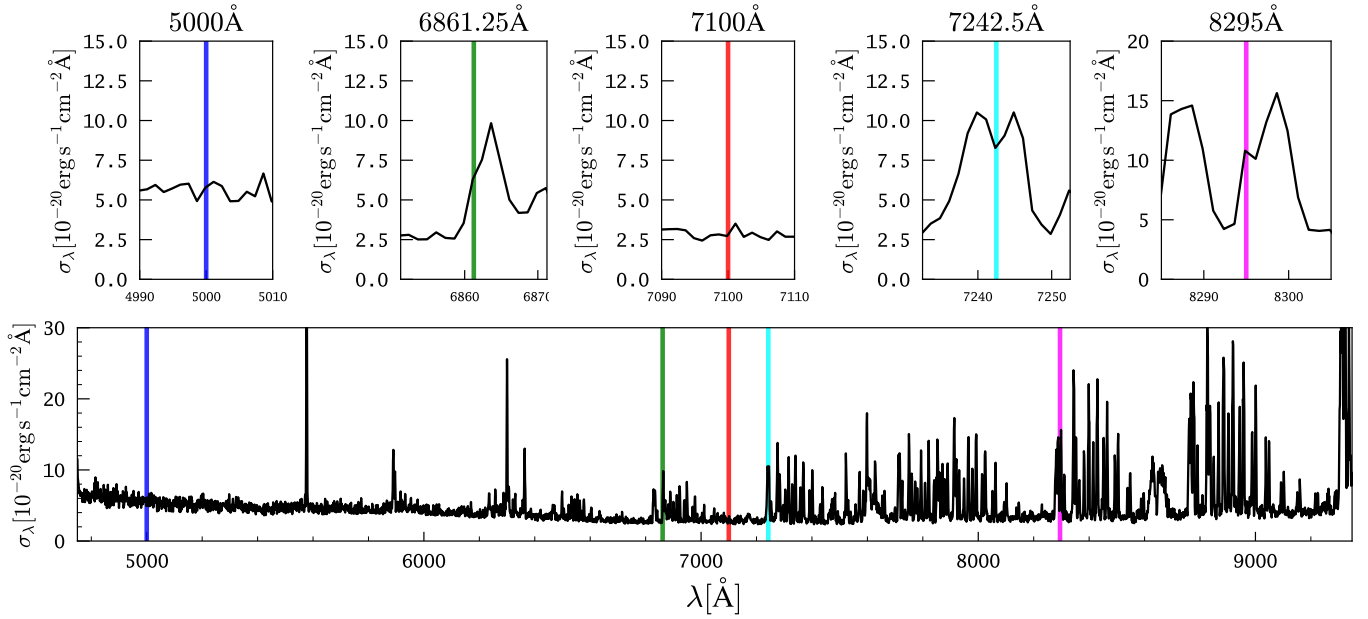


Fig. 2. Insertion wavelengths for completeness function estimation. *Bottom panel:* the background noise over the whole spectral range; the vertical lines indicate the positions of the artificially implanted LAEs. *Top panel:* zoomed-in versions around the regions of interest. The colours of the vertical lines correspond to the colours used for the source recovery fractions in Figs. 3–5.

3.1. Source recovery experiment with artificial point sources

We first computed recovery fractions for an oversimplified case where we assumed that LAEs are perfect point sources with simple spectral profiles. In particular we modelled the light profiles of the implanted sources with a Moffat function (Moffat 1969). This parameterisation provides a reasonably good approximation of the seeing-induced PSF in ground-based optical to near-infrared observations (Trujillo et al. 2001). To account for the wavelength dependence of the full width at half maximum (FWHM) of the PSF, we used the coefficients of linear fits of $\text{FWHM}(\lambda)$ provided in Table 2 of H017. The spectral profile of the fake sources is modelled as a simple Gaussian of 250 km s width (FWHM).

As it is computationally not feasible to perform the source insertion and recovery experiment for all wavelength layers in each of the 24 MW datacubes, we selected five insertion wavelengths that are representative of typical noise situations in the datacube (see Fig. 2): $\lambda_1 = 5000 \text{ \AA}$, $\lambda_2 = 6861.25 \text{ \AA}$, $\lambda_3 = 7100 \text{ \AA}$, $\lambda_4 = 7242.5 \text{ \AA}$, and $\lambda_5 = 8292.5 \text{ \AA}$. In particular, the spectral regions around 5000 \AA and 7100 \AA are typical regions devoid of night sky line emission, while 6861.25 \AA is in the wing of a sky line, and the 7242.5 \AA and 8292.5 \AA positions are chosen to be right between two neighbouring sky lines. At these insertion wavelengths we then populate each of the 24 MW cubes with $N_{\text{tot}} = 64$ fake sources at different spatial positions. Instead of placing the inserted sources on a regular grid, we used a quasi-random grid based on a Sobol sequence (see e.g. Sect. 7.7 of Press et al. 1992). This is done to avoid placement of the sources at similar distances to the edges of the MUSE slice stacks. These stacks are arranged in a rectangular pattern, which is only slightly modulated by the small dither offsets during the observations. With this procedure we ensured that our selection function is not affected by systematic defects that are known to exist at the slice stack edges (see e.g. Fig. 3 in Bacon et al. 2017). We then inserted fake sources with 20 different flux levels from $\log F_{\text{Ly}\alpha} [\text{erg s}^{-1} \text{ cm}^{-2}] = -17.5$ to $\log F_{\text{Ly}\alpha} [\text{erg s}^{-1} \text{ cm}^{-2}] =$

-15.5 in steps of 0.1 dex at the five chosen wavelength layers into each MW datacube. The $20 \times 24 = 480$ datacubes were then continuum subtracted with the running median filter as described in Sect. 2.2. We then process these continuum subtracted cubes with LSDCat in the same way as for the original catalogue construction (Sect. 2.2). In order to decrease the computational cost for this experiment, we trimmed the continuum subtracted fake-source populated datacubes by $\pm 30 \text{ \AA}$ around each insertion wavelength. For each subcube we then counted the number sources N_{det} that are recovered by LSDCat above the same detection threshold ($S/N_{\text{det}} = 8$) that was used for the creation of the MW emission line source catalogue (see Sect. 2.2). As an example, we show in Fig. 3 the resulting recovery fractions for each insertion wavelength for MW pointing 01. We note that the shape and order of the curves is similar for all other pointings.

3.2. Source recovery experiment with real LAEs

We also performed a source insertion and recovery experiment using the 10 LAEs from the MUSE HDFS catalogue that have the highest S/N (MUSE HDFS ID 43, 92, 95, 112, 139, 181, 246, 325, 437, and 547 all have $S/N > 10$). These sources show a range of different surface-brightness profiles: e.g. while the LAEs 43, 92, and 95 are fairly extended, the LAEs 181, 325, and 542 show more compact surface brightness profiles (Wisotzki et al. 2016). They also represent a range of fluxes, redshifts, and line profiles. Given their high S/N in the MUSE HDFS data, they are practically noise free compared to the noise level in MW, even when being multiplicatively rescaled to higher flux levels. We compare the fluxes and redshifts of these ten LAEs to the actual MUSE-Wide sample in Fig. 1. It can be seen that all MUSE HDFS LAEs used in the source insertion experiment could potentially be part of the MW Sample.

We rescaled these LAEs to 20 different flux levels between $\log F_{\text{Ly}\alpha} [\text{erg s}^{-1} \text{ cm}^{-2}] = -17.5$ to $\log F_{\text{Ly}\alpha} [\text{erg s}^{-1} \text{ cm}^{-2}] = -15.5$ in steps of 0.1 dex (i.e. we used the same flux levels as before for the simplified sources). For this purpose we first

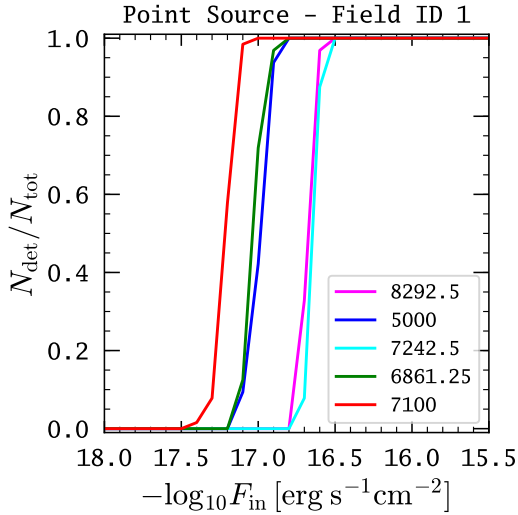


Fig. 3. Recovery fraction $N_{\text{det}}/N_{\text{total}}$ from a source insertion and recovery experiment for simplified point-like emission sources at five different wavelengths (see Fig. 2) in the MW pointing 01 datacube. $N_{\text{total}} = 64$ is the number of inserted sources at a given flux level and N_{det} is the number of recovered sources for a given line flux F_{in} obtained with same detection procedure used to construct the original MW catalogue.

measured the fluxes from the MUSE HDFS LAEs by utilising the LSDCat flux-measurement routine with circular apertures of radius $3R_{\text{Kron}}$. We then cut out mini cubes from the MUSE HDFS datacube that are centred on the LAEs. The voxels in these mini-cubes were then multiplied by constant factors to reach the desired flux levels. These 20×10 (flux samples \times source samples) “fake-source” mini cubes were inserted into each of our 24 MW datacubes at the five different insertion wavelengths and at the same positions that were used for the simplified sources.

When inserting the sources at different wavelengths we accounted for the redshift broadening of spectral profile, i.e. we kept the profile shape fixed in velocity space. We also needed to account for the differences in the PSF between MW and MUSE HDFS. Since in all MW datacubes the PSF is broader than it is in the HDFS, we have to degrade the PSF of the inserted mini cubes. To this end we convolved their spatial layers with a 2D Gaussian of dispersion $\sigma_{2D}(\lambda) = \sqrt{\sigma_{\text{MW}}(\lambda)^2 - \sigma_{\text{HDFS}}(\lambda)^2}$, where $\sigma_{\text{MW}}(\lambda)$ and $\sigma_{\text{HDFS}}(\lambda)$ are the wavelength-dependent PSF dispersions of a MUSE-Wide datacube and the MUSE HDFS datacube, respectively. Here the MUSE HDFS PSF was determined from fits to the brightest star in the field (see Fig. 2 of Bacon et al. 2015), while the linear model of H017 was used for the MW PSF.

After having continuum subtracted datacubes with artificially implanted sources, the next step was to perform the recovery experiment. To reduce the computational cost of this experiment, we trimmed the fake-source inserted cubes in wavelength range to $\pm 30 \text{ \AA}$ around each insertion wavelength. The full recovery experiment was thus performed on $20 \times 10 \times 5 \times 24 = 24\,000$ datacubes of dimensions $\sim 300 \times 300 \times 50$ (neglecting empty edges due to the rotation of the MW pointings). Each of these cubes was processed with LSDCat using the same parameters that were used to generate the catalogue of LAEs in the 24 MW fields. We then counted the number of recovered sources N_{det} above the same detection threshold that was used in the creation of the MW LAE source catalogue ($S/N_{\text{det}} = 8$).

We demonstrate the outcome of the recovery experiment with realistic LAES for the MW pointing 01 datacube in Fig. 4,

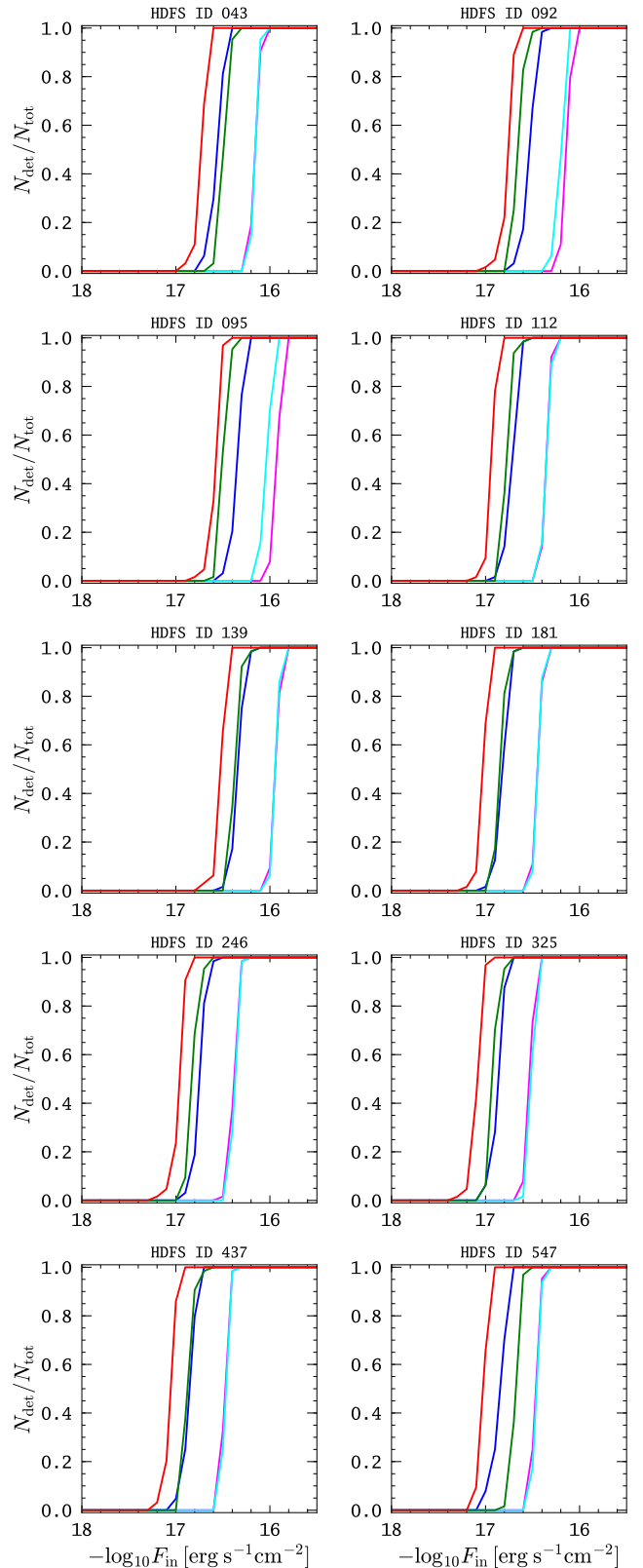


Fig. 4. Recovery fractions from a source insertion and recovery experiment with ten MUSE HDFS LAEs for MW datacube 01. Each panel displays the recovery fraction $N_{\text{det}}/N_{\text{total}}$ for a particular MUSE HDFS LAE as a function of its scaled flux at five different wavelengths (see Fig. 2). N_{total} and N_{det} are as defined in Fig. 3.

noting that the results for the other datacubes are similar. We found that the completeness curves for all emitters have a very

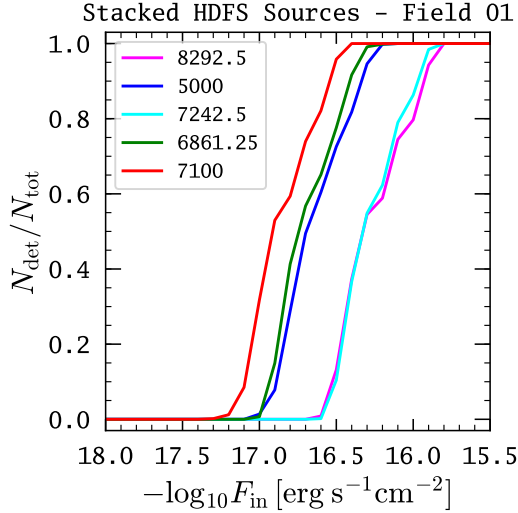


Fig. 5. Stack over the recovery fractions $N_{\text{det.}}/N_{\text{total}}$ of the ten different MUSE HDFS LAEs used in the source recovery experiment. These curves represent the selection function at five different wavelengths in a MW datacube. We only show the results for the MW datacubes 01; the shape of the curves are similar for all other fields.

steep cut-off at line fluxes of $10^{-16} \dots 10^{-17} \text{ erg s}^{-1} \text{ cm}^{-2}$. While for the more compact LAEs the cut-off is comparable to that obtained for the idealised sources (see Fig. 3), for the more extended LAEs it is significantly shifted to brighter flux levels. The exact turnover point on a given curve appears to be a complicated function of a source’s surface-brightness profile and its spectral profile. However, we observe that for a given source all curves are self-similar and the shift depends only on the insertion wavelength (Fig. 2). Since the ten LAEs from the MUSE HDFS used in the recovery experiment are expected to be a representative subset of the overall high- z LAE population, we expect the overall LAE selection function at a specific wavelength to be the average recovery fraction over all sources $\langle N_{\text{det.}}/N_{\text{tot.}} \rangle$ at this wavelength. In Fig. 5 we show as an example these averaged recovery fractions for MW pointing 01. Similar to the idealised sources, the shape and the order of the curves is similar for all other pointings.

3.3. From recovery fractions to selection functions

Up to this point we are equipped with LAE selection functions for the MW LAEs only at five different wavelengths within the MUSE wavelength range. However, we notice in Figs. 3 and 5 that the curves at the different wavelengths are self-similar and that their order in flux is always the same. This result indicates that there is a universally shaped selection function whose shift with respect to the flux axis is determined by a wavelength dependent quantity. Indeed, we found that the shift of the 50% completeness point ($f_C(F_{50}) = 0.5$) of the determined curves shows a nearly constant F_{50} -to- $\tilde{\sigma}_{\text{emp}}$ ratio for all curves, with $\tilde{\sigma}_{\text{emp}}$ being the empirically determined background noise convolved with a 250 km s^{-1} wide (FWHM) Gaussian. The ratio $F_{50}/\tilde{\sigma}_{\text{emp}}(\lambda)$ varied between 400 and 460 for the different datacubes; the exact value depended on the average datacube background noise and is a function of the observing conditions. Using this scaling we could compute $f_{C,i}(F_{\text{Ly}\alpha}, \lambda)$ for each of the 24 MW pointings (here i indexes the pointing). We created a master $f(F)$ -curve from shifting the five stacked curves on top of each other by requiring them to have the same

$f_C(F'_{50}) = 0.5$ value. For each wavelength bin we then shifted this $f(F)$ -master curve according to the $F_{50}/\tilde{\sigma}_{\text{emp}}(\lambda)$ proportionality to obtain $f_{C,i}(F_{\text{Ly}\alpha}, \lambda)$. The final selection functions for the MW LAE catalogue were then the average of all 24 selection functions.

The resulting selection function for the point-like emission line sources is called the point source selection function (PSSF). This more realistic selection function is therefore called the real source selection function (RSSF). Both selection functions are shown in Fig. 6 in redshift-flux space⁹ and in Fig. 7 redshift-luminosity space.

The PSSF can be seen as a limiting depth of our survey since it resembles closely the template of the matched filter used in the emission line source detection H017. More importantly, in comparison to the RSSF it also demonstrates the loss in sensitivity in LAE surveys due to the fact that these sources are not compact, but exhibit significant low surface brightness halo components. Moreover, while the transition from 0% to 100% completeness is quite rapid for the PSSF, the variety of Ly α halo properties encountered amongst LAEs leads to a much smoother transition. Notably, in extreme cases Ly α halos can contain up to 90% of the total Ly α flux (Wisotzki et al. 2016; Leclercq et al. 2017). Therefore, the assumption of point-like LAEs in estimating the selection function leads to an overestimate of survey depth. While Grove et al. (2009) already noted this effect, they were not able to robustly quantify it due to the lack of deeper comparison data.

4. Deriving the Lyman α luminosity function

Before presenting the results of the LAE LF in the next section, we provide here an overview of the methods used to derive the LAE LF in our integral field spectroscopic dataset.

We use three different non-parametric LF estimators: the classical $1/V_{\text{max}}$ method (Sect. 4.1.1), a binned alternative method to $1/V_{\text{max}}$ introduced by Page & Carrera (2000; Sect. 4.1.2), and the C^- method (Sect. 4.1.3). As we discuss, the second and third method provide some advantages over the classical $1/V_{\text{max}}$ approach. Moreover, we also make use of a non-parametric method to test the redshift evolution of the LAE LF (Sect. 4.1.4). Furthermore, photometric uncertainties at low completeness levels will lead to biases in the LF estimate. In order to avoid those biases we truncate the sample and define appropriate luminosity bins for the binned estimators. We motivate our truncation criterion and bin-size choice in Sect. 4.2. Finally, in Sect. 4.3 we explain the maximum-likelihood fitting formalism that we employ to derive parametric models of the LAE LF.

4.1. Non-parametric luminosity function estimates

4.1.1. The $1/V_{\text{max}}$ method

The first non-parametric LF estimator we consider is the $1/V_{\text{max}}$ estimator (Schmidt 1968; Felten 1976) in a modified version to account for a complex, i.e. redshift- and luminosity-dependent, selection function (Fan et al. 2001; Caditz 2016).

The $1/V_{\text{max}}$ estimator approximates the cumulative luminosity function

$$\Phi(L_{\text{Ly}\alpha}) = \int_{L_{\text{Ly}\alpha}}^{\infty} \phi(L'_{\text{Ly}\alpha}) dL'_{\text{Ly}\alpha}, \quad (4)$$

⁹ The LAE selection functions shown in Fig. 6 (RSSF and PSSF) are made available as associated data products via the CDS.

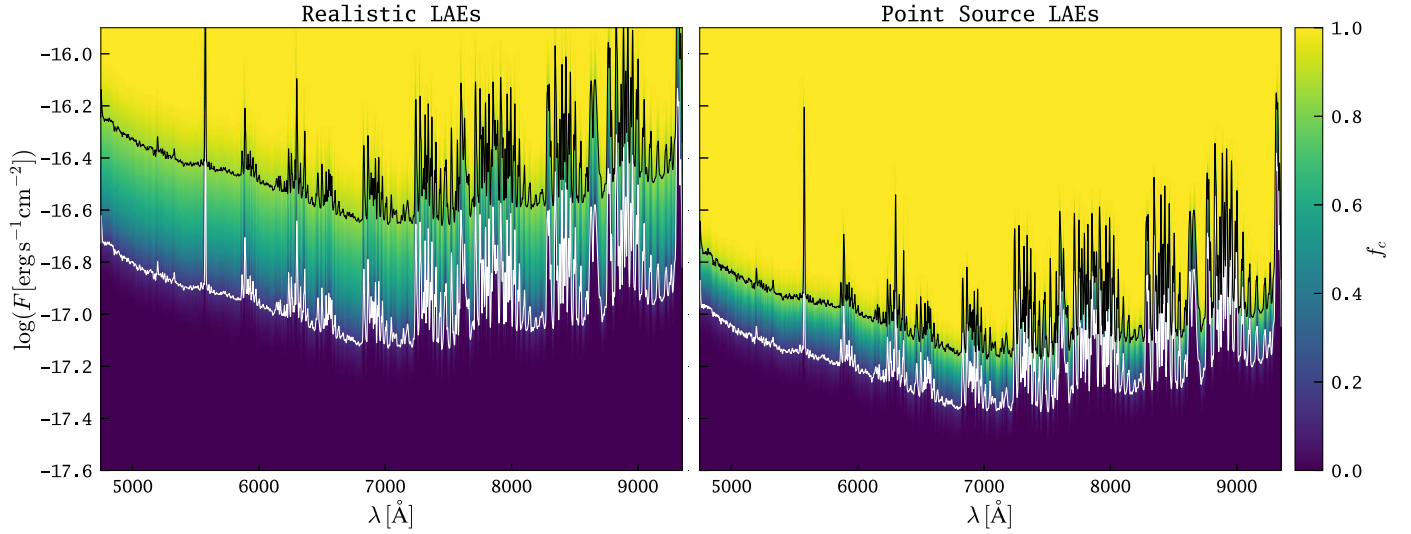


Fig. 6. Selection function $f_c(F_{Ly\alpha}, \lambda)$ for LAEs in the MW survey. The white and black lines indicate the 15% and 85% completeness limits, respectively. *Left panel:* RSSF (see Sect. 3.2). *Right panel:* PSSF (see Sect. 3.1).

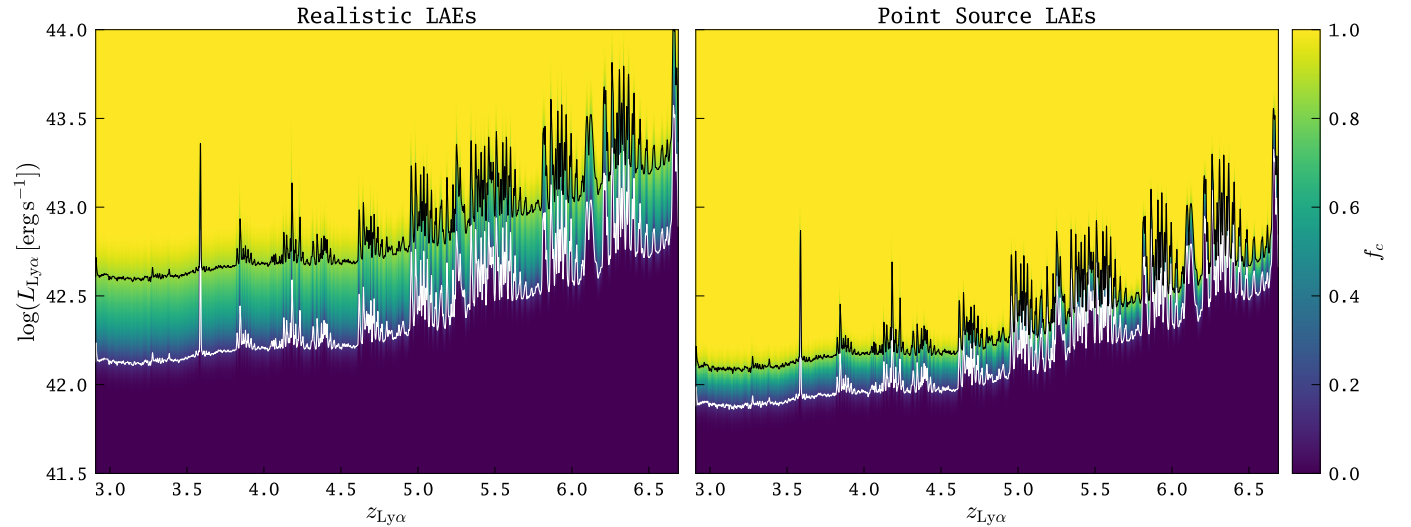


Fig. 7. Selection function for LAEs in the MW survey, similar to Fig. 6, but now transformed to redshift-luminosity space.

where $\phi(L_{Ly\alpha})$ is the differential LF introduced in Eq. (1), via

$$\Phi(L_{Ly\alpha,k}) = \sum_{i \leq k} \frac{1}{V_{\max,i}}. \quad (5)$$

Here, and in the following, we assume that the objects are ordered in Ly α luminosity, i.e.

$$L_{Ly\alpha,1} > L_{Ly\alpha,2} > \dots > L_{Ly\alpha,N-1} > L_{Ly\alpha,N}. \quad (6)$$

In Eq. (5) $V_{\max,i}$ denotes the maximum volume accessible for each LAE i in the survey. In the presence of our redshift-dependent selection function $f_c(L, z)$ (Fig. 7) we can write

$$V_{\max,i} = \omega \int_{z_{\min}}^{z_{\max}} f_c(L_{Ly\alpha,i}, z) \frac{dV}{dz} dz \quad (7)$$

(e.g. Wisotzki 1998; Johnston 2011). Here ω is the angular area of the survey ($\omega = 22.2$ arcmin² for the 24 fields of the first instalment of the MW survey under consideration here), $\frac{dV}{dz}$ is the differential cosmological volume element¹⁰, and z_{\min} (z_{\max})

¹⁰ For a definition of $\frac{dV}{dz}$, see e.g. Hogg (1999).

denotes the lower (upper) limit of the redshift range under consideration¹¹.

Moreover, in the $1/V_{\max}$ formalism the differential LF can be approximated by the binned estimator

$$\phi_{1/V_{\max}}(\langle L_{Ly\alpha} \rangle) = \frac{1}{\Delta L_{Ly\alpha}} \sum_k \frac{1}{V_{\max,k}}, \quad (8)$$

where $\langle L_{Ly\alpha} \rangle$ is the average Ly α luminosity of a bin, $\Delta L_{Ly\alpha}$ is the width of the bin, and the sum runs over all sources k in that bin. The uncertainty for each bin is defined as

$$\Delta\phi_{1/V_{\max}}(\langle L_{Ly\alpha} \rangle) = \sqrt{\frac{1}{\Delta L^2} \sum_i \frac{1}{V_{\max,i}^2}} \quad (9)$$

(e.g. Johnston 2011).

¹¹ In our study these limits are either imposed by the full spectral coverage of MUSE, i.e. $(z_{\min}, z_{\max}) = (2.9, 6.7)$, or by the redshift bins that we consider (see Table 1).

4.1.2. Binned estimator proposed by Page & Carrera (2000)

The second non-parametric estimator we consider provides an alternative binned estimate for the differential LF. In its original form it was proposed by Page & Carrera (2000). Following Yuan & Wang (2013), who provide a thorough comparison with the $1/V_{\max}$ method, we call it the ϕ_{PC} estimator. This estimator was motivated by potential systematic biases in the $1/V_{\max}$ estimator close to the flux limit of the survey. It has not yet been utilised to derive LAE LFs.

Instead of considering the maximum volume accessible for each individual source in the binned $1/V_{\max}$ estimator (Eq. (8)), Page & Carrera (2000) argue that it is more robust to consider the average four-dimensional volume in redshift-luminosity space for each bin and then to divide the number of sources present in the bin by this hypervolume. In the presence of a redshift-dependent selection function we can write the ϕ_{PC} estimator as

$$\phi_{\text{PC}}(\langle L_{\text{Ly}\alpha} \rangle) = \frac{N}{\omega \int_{L_{\min}}^{L_{\max}} \int_{z_{\min}}^{z_{\max}} f_c(L_{\text{Ly}\alpha}, z) \frac{dV}{dz} dz dL}, \quad (10)$$

where again $\langle L_{\text{Ly}\alpha} \rangle$ denotes the average Ly α luminosity of a bin, z_{\min} and z_{\max} are the limits of the redshift range under consideration, L_{\min} and L_{\max} are the lower and upper bounds of the bin in which the LF is estimated, and N is the number of sources within the bin. In analogy to Eq. (9), we estimate the statistical uncertainty on $\phi_{\text{PC}}(\langle L_{\text{Ly}\alpha} \rangle)$ by replacing N with \sqrt{N} in Eq. (10).

4.1.3. The C^- method

We also consider the C^- method for estimating the cumulative LF defined in Eq. 4. This method was introduced into the astronomical literature by Lynden-Bell (1971) and the generalisation for complex selection functions was introduced by Petrosian (1992). To date, the generalised C^- method has not been used to derive LAE LFs. Formal derivations of the method in the presence of a redshift- and luminosity-dependent selection function are given elsewhere (e.g. Fan et al. 2001; Johnston 2011; Caditz 2016); here we just summarise the computational algorithm¹².

The first step in the generalised C^- method is to define the generalised comparable set J_i for each LAE i that contains all LAEs j with higher Ly α luminosity:

$$J_i = \{j : L_j > L_i\}. \quad (11)$$

The next step is to make a weighted count of the number of LAEs in each comparable set

$$T_i = \sum_{j=1}^{N_i} w_j, \quad (12)$$

where N_i is the number of LAEs in the comparable set J_i . The weights w_j for each object j in J_i are given by the selection probability if the J_i -defining object i with its Ly α luminosity $L_{\text{Ly}\alpha,i}$ had been detected at the redshift of an object j , $f_c(L_{\text{Ly}\alpha,i}, z_j)$, normalised by j 's actual selection probability $f_c(L_{\text{Ly}\alpha,j}, z_j)$, i.e.

$$w_j = \frac{f_c(L_{\text{Ly}\alpha,i}, z_j)}{f_c(L_{\text{Ly}\alpha,j}, z_j)}. \quad (13)$$

Since by construction $L_{\text{Ly}\alpha,j} > L_{\text{Ly}\alpha,i}$, and since f_c is monotonically increasing with luminosity at a given redshift, $w_j \leq 1$ holds.

¹² An introduction into the C^- method is also presented in Chapter 4.9.1. of the Ivezić et al. (2014) textbook.

With these weighted counts the cumulative LAE LF is given as

$$\Phi(L_{\text{Ly}\alpha,k}) = \Phi(L_{\text{Ly}\alpha,1}) \prod_{i=2}^k \left(1 + \frac{1}{T_i}\right), \quad (14)$$

where the normalisation $\Phi(L_{\text{Ly}\alpha,1})$ has to be determined separately (see Sect. 4.1.4).

A potential advantage of the C^- method over the $1/V_{\max}$ method is that it only requires evaluation of the selection function at redshifts where sources were actually detected, whereas the calculation of the LF using the $1/V_{\max}$ method requires integration over the selection function for the whole redshift range of interest.

Caditz (2016) provides a detailed formal comparison between the C^- and $1/V_{\max}$ estimators, showing that both are asymptotically unbiased, i.e. both $1/V_{\max}$ and C^- yield a correct estimate of the true luminosity function for large number of objects and a correct estimate of the selection function. However, the main difference between the two estimators is that $1/V_{\max}$ is more sensitive to uncertainties in the selection function, while C^- is more sensitive to random fluctuations in the sample.

4.1.4. Non-parametric test for LF evolution

The $1/V_{\max}$ method as formulated in Sect. 4.1.1 explicitly assumes that the LF is non-evolving over the redshift range under consideration, whereas the key assumption in the C^- method described above is that the distribution function $\Psi(L, z)$, which describes a potentially evolving LF as a scalar field in redshift-luminosity space, is separable, i.e.

$$\psi(L, z) = \rho(z)\phi(L). \quad (15)$$

Here $\rho(z)$ describes the mean density of sources as a function of redshift. Thus, if Eq. (15) is an adequate description of the evolving LF, then $\phi(L)$, and correspondingly $\Phi(L)$, would retain its shape over the redshift range under consideration, with only the overall normalisation being allowed to change.

The assumption of an LF evolving according to Eq. (15) is commonly referred to as pure density evolution. In principle, $\rho(z)$ can also be determined with the formalism described above, by just exchanging redshifts with luminosities of object i in Eq. (12) and then using Eq. (14) to estimate $\rho(z)$. While such a derivation could be used to normalise the cumulative LF from the C^- method, here we take the shortcut by utilising $\Phi(L_{\text{Ly}\alpha,1})$ from the $1/V_{\max}$ method in Eq. (14),

$$\Phi(L_{\text{Ly}\alpha,1}) = \frac{1}{V_{\max,1}}, \quad (16)$$

i.e. we implicitly assume that ρ is constant over the redshift ranges under consideration.

Following Fan et al. (2001), we test the validity of the pure density evolution of the LAE LF in the luminosity range probed by our survey with the statistical test developed by Efron & Petrosian (1992). We calculate for each J_i the generalised rank R_i of z_i :

$$R_i = \sum_{j=1}^{N_i} w_j \Theta(z_i - z_j), \quad \text{with } \Theta(x) = \begin{cases} 0 & \text{for } x < 0 \\ 1 & \text{for } x \geq 0. \end{cases} \quad (17)$$

If z is independent of L in the sense of Eq. (15), then the R_i values should be distributed uniformly between 0 and the corresponding T_i values, i.e. the expectation value of R_i is $E_i = T_i/2$ and its

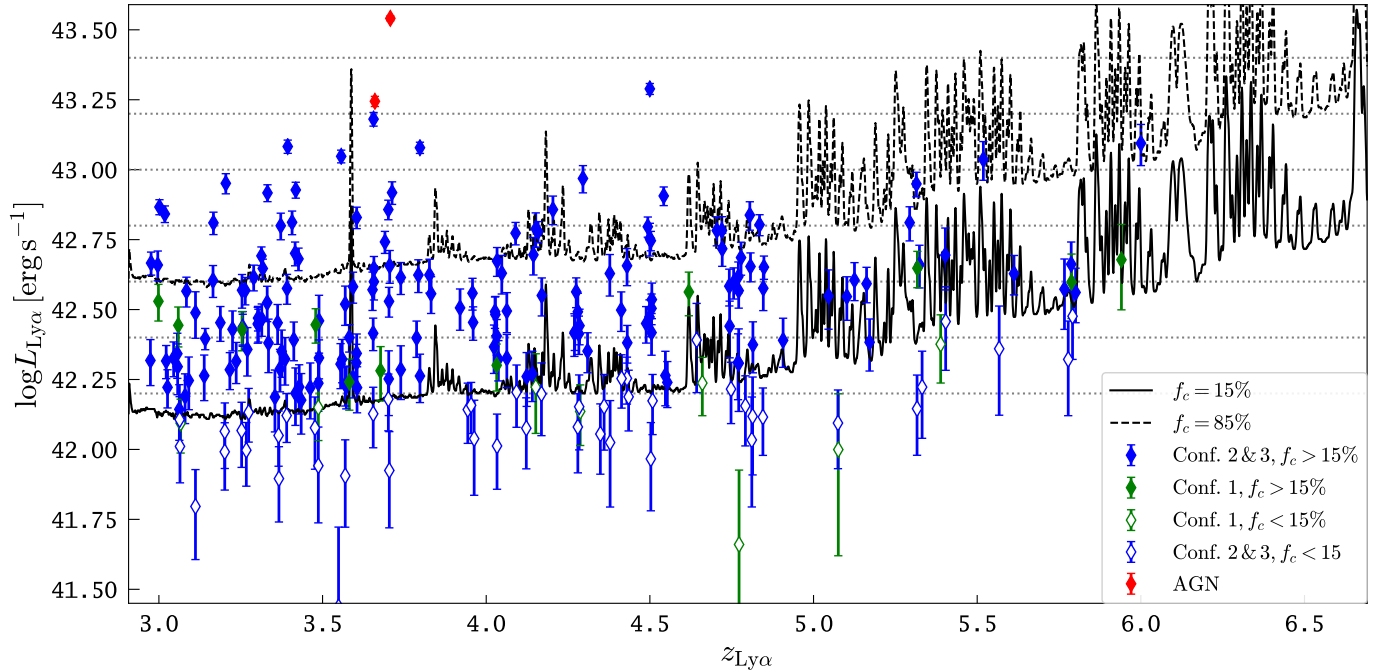


Fig. 8. LAE sample of the first 24 MW pointings in redshift-luminosity space. The dashed line represents the 85% RSSF completeness limit, while the black line denotes the 15% RSSF completeness limit at which we truncate our sample leaving 179 of 237 (75.6%) LAEs. Individual emitters are colour-coded according to their assigned confidence flags (blue: little to no doubt on being an LAE; green: LAEs flagged as uncertain; for details on assigning the confidence values, see Sect. 3.2 of H017). The two highest $L_{\text{Ly}\alpha}$ objects are AGN indicated by red symbols. Sources below the truncation line are shown with open symbols. Horizontal dotted lines denote the adopted bin boundaries ($\log L_{\text{Ly}\alpha, \text{bin}} [\text{erg s}^{-1}] = 42.2 + i \times 0.2$ for $i = 0, 1, \dots, 5$) for the binned LAE LF estimates.

variance is $V_i = T_i^2/12$. Moreover, the statistic

$$\tau = \frac{\sum_i (R_i - E_i)}{\sqrt{\sum_i V_i}} \quad (18)$$

is approximately a standard normal distribution under the null hypothesis that independence between z and L in Eq. (15) is valid.

We follow the literature by adopting $|\tau| < 1$ as the critical value at which the independence assumption cannot be rejected (Efron & Petrosian 1992; Fan et al. 2001). We point out that for a standard normal distribution this value corresponds to p -values $p_0 > 0.16$, i.e. it is decidedly higher than commonly adopted significance levels to reject the null hypothesis (e.g. $p_0 < 0.05$ for 1σ).

4.2. Truncation and binning of the sample

Non-parametric estimates of the differential luminosity function, regardless of the estimator used, require binning of the sample in luminosities. Moreover, at the faintest luminosities the photometric uncertainties become so large that they would translate into a large uncertainties for the completeness correction in the LF estimation. This potential bias can be avoided by trimming the sample from such sources. We visualise our choice of bin sizes and truncation limit for the RSSF in Fig. 8.

We curtail the sample from sources that are detected below the $f_c = 0.15$ completeness limit. As can be seen in Fig. 8, the vast majority of LAEs below the $f_c = 0.15$ limit have photometric errors that extend below the 0% completeness line, which provides the main motivation for this truncation limit. This truncation limit removes 54 LAEs from the initial MW LAE sample for the RSSF. In the calculation of the luminosity function,

we account for the truncation limit by setting $f_c \equiv 0$ for all $f_c < 0.15$.

We chose our lowest luminosity boundary to be $\log L_{\text{Ly}\alpha} [\text{erg s}^{-1}] = 42.2$, motivated by the fact that it straddles our RSSF truncation criterion in the $z \lesssim 5$ region in the sample (Fig. 8). However, as we opt for a single decimal place, this removes four additional objects from the LF sample truncated according to the RSSF. For the PSSF all sources except one have $f_c > 0.15$ above $\log L_{\text{Ly}\alpha} [\text{erg s}^{-1}] = 42.2$. We chose our adopted bin-size $\Delta \log L_{\text{Ly}\alpha} [\text{erg s}^{-1}] = 0.2$ because it is significantly larger than the photometric error in the lowest luminosity bin. Moreover, we show in Sect. 5.2 that for this bin-size the non-parametric estimates are in optimal agreement with the parametric maximum-likelihood solution.

Although estimating the binned differential LF is popular in the literature, we point out that binning represents a loss of information¹³, while all information present in the source catalogue is retained when deriving the cumulative LF (Felten 1976; Caditz 2016). Moreover, the adopted maximum-likelihood procedure (see Sect. 4.3) does not require binning of the data. Here we use the binned estimates only for visual comparison to the binned values from the literature in combination with our derived Schechter parameterisation (see Sect. 7).

4.3. Parametric maximum likelihood luminosity function estimation

In order to obtain a parametric description of the MW LAE LF we use the maximum likelihood parameter estimation approach

¹³ A recent discussion of the pitfalls when using binning in the analysis of astronomical data was presented in Steinhart & Jermyn (2018).

introduced by Sandage et al. (1979) into the field of observational cosmology. Maximum likelihood estimation is a statistical technique used to estimate the parameters of a model given the data. We therefore need to assume an analytical expression for the LF. The Schechter function (Schechter 1976) is the most commonly adopted functional form for the Ly α LF:

$$\phi(L) dL = \phi^* \left(\frac{L}{L^*}\right)^\alpha \exp\left(-\frac{L}{L^*}\right) \frac{dL}{L^*}. \quad (19)$$

We obtain the free parameters L^* (characteristic luminosity in erg s^{-1}), α (faint-end slope), and ϕ^* (normalisation in Mpc^{-3}) by maximising the likelihood function

$$\mathcal{L} = \prod_{i=1}^{N_{\text{LAE}}} p(L_i, z_i), \quad (20)$$

where

$$p(L_i, z_i) = \frac{\phi(L_i) f_c(L_i, z_i)}{\int_{L_{\min}}^{L_{\max}} \int_{z_{\min}}^{z_{\max}} \phi(L) f_c(L, z) \frac{dV}{dz} dL dz} \quad (21)$$

(e.g. Sandage et al. 1979; Fan et al. 2001; Johnston 2011). In practice we search for the minimum of

$$S = -2 \times \ln \mathcal{L}. \quad (22)$$

Evaluation of this equation thus requires a summation over the entire unbinned sample. As can be seen in Eq. (21), the space density scaling factor ϕ^* cancels out and is thus not really a free parameter in the fitting process. For any given combination of L^* and α the value of ϕ^* is, however, uniquely determined since the integral in the denominator must equal the total number of objects in the sample used to calculate the likelihood function (e.g. Mehta et al. 2015).

Even simpler than a Schechter function is a power-law distribution of

$$\phi(L) dL = \frac{\phi^*}{L^*} \times L^\beta dL, \quad (23)$$

which lacks the exponential cut-off and thus implies a larger fraction of high-luminosity objects for equal power-law indices $\beta = \alpha$. Comparing Eq. (23) to Eq. (21) it becomes evident that only β is a free parameter in the likelihood function, but as above the ratio ϕ^*/L^* is uniquely constrained by the total number of objects.

We do not consider more complex parametric expressions for the Ly α LF such as a double power law because, as demonstrated in Sect. 5.2, they are not required for our data.

5. Results of the Lyman α luminosity function

5.1. Non-parametric reconstructions of the LAE LF

We first employed the non-parametric statistical test described in Sect. 4.1.4 to investigate whether the observed MW LAE LF is consistent with a pure density evolution scenario. Table 1 lists the obtained τ -values from Eq. (18) along with the corresponding p -values under the normal distribution approximation. We calculated τ both for the RSSF and the PSSF. Moreover, we tested evolution not only for the full MW redshift range, but also within three redshift ranges: $2.9 < z \leq 4$, $4 < z \leq 5$, and $5 < z \leq 6.7$. Regardless of the adopted selection function, we find that the pure density evolution scenario cannot be rejected over the full redshift range (i.e. $|\tau| < 1$, thus $p_0 > 0.16$), or over the three redshift ranges. This means that over the dynamic range

Table 1. Results of statistical test according to Eq. (18) for testing the assumption of pure density evolution as defined in Eq. (15).

Redshift range	$ \tau_{\text{PSSF}} $	$ \tau_{\text{RSSF}} $	p_{PSSF}	p_{RSSF}
$2.9 < z \leq 4$	0.47	0.24	0.32	0.40
$4.0 < z \leq 5.0$	0.79	0.98	0.21	0.16
$5.0 < z \leq 6.7$	0.05	0.29	0.48	0.39
$2.9 < z \leq 6.7$	0.46	0.31	0.32	0.38

Notes. τ values were computed for the point source selection function (τ_{PSSF}) and the selection function accounting for extended Ly α emission (τ_{RSSF}). The corresponding values of p for a standard normal distribution are given in Cols. 3 and 4.

of probed Ly α luminosities the shape of the observed LAE LF remains unchanged at $3 \lesssim z \lesssim 5$. The test, however, is not sensitive for a possible change in the normalisation. However, we demonstrate below (see especially Fig. 16) that such a change in normalisation is also not required for the observed LAE LF.

A non-evolving apparent LAE LF is consistent with the result from the NB imaging survey by Ouchi et al. (2008). This study found no significant differences between the apparent LAE LF (i.e. uncorrected for Ly α absorption by the intergalactic medium) in their three surveyed redshift slices ($z \approx \{3.1, 3.7, 5.7\}$). On the other hand, at first our result appears to be in tension with the recently reported LAE LF evolution from $z \approx 2.5$ to $z \approx 6$ within the SC4K survey (Sobral et al. 2018a), but the change in the SC4K LAE LFs is driven by a decreasing number density of the highest luminosity LAEs ($\log L_{\text{Ly}\alpha} [\text{erg s}^{-1}] \gtrsim 43.0$). Unfortunately, with the current MW data we do not sample a large enough number of luminous LAEs to obtain a statistically robust confirmation of this result. Moreover, the current MW sample is also not well populated with $z \gtrsim 5.5$ LAEs. Thus, to date, we also cannot add constraints to the ongoing debate in the literature regarding a possible LAE LF evolution between $z = 5.7$ and $z = 6.6$ (Ouchi et al. 2010; Santos et al. 2016; Konno et al. 2018).

We now analyse the differences in the resulting LAE LF when employing the two different selection functions constructed in Sect. 3. To this end we plot in Fig. 9 the resulting cumulative LAE LFs obtained with the C^- method (Sect. 4.1.3) for the RSSF, which explicitly accounts for the extended low surface brightness halos of LAEs (left panel in Fig. 6), and for the PSSF, which assumes LAEs to be compact PSF broadened sources (right panel in Figs. 6 and 7). We find that at the faint end of our probed luminosity range ($\log L_{\text{Ly}\alpha} [\text{erg s}^{-1}] = 42.2$) the inferred LAE density utilising the RSSF is a factor of 2.5 higher compared to the PSSF: $\Phi_{\text{RSSF}}(\log L_{\text{Ly}\alpha} [\text{erg s}^{-1}] = 42.2) = 2 \times 10^{-3} \text{ Mpc}^{-3}$, while $\Phi_{\text{PSSF}}(\log L_{\text{Ly}\alpha} [\text{erg s}^{-1}] = 42.2) = 8 \times 10^{-4} \text{ Mpc}^{-3}$.

We argue that due to the ubiquity of extended Ly α emission around LAEs, the RSSF represents a more realistic selection function. Hence, we regard the LAE LF constructed with this completeness correction as unbiased. Since previous LAE LF determinations, except Drake et al. (2017b), have not accounted for an extended nature of LAEs in their selection functions, we expect similar biases in their inferred number densities close to their limiting luminosities. We demonstrate in Sect. 6 that our PSSF completeness-corrected Ly α LF agrees better with most literature estimates. Therefore, we note that our PSSF LAE LF estimates here only serve demonstrative purposes, while the RSSF corrected estimate can be regarded as our best estimate.

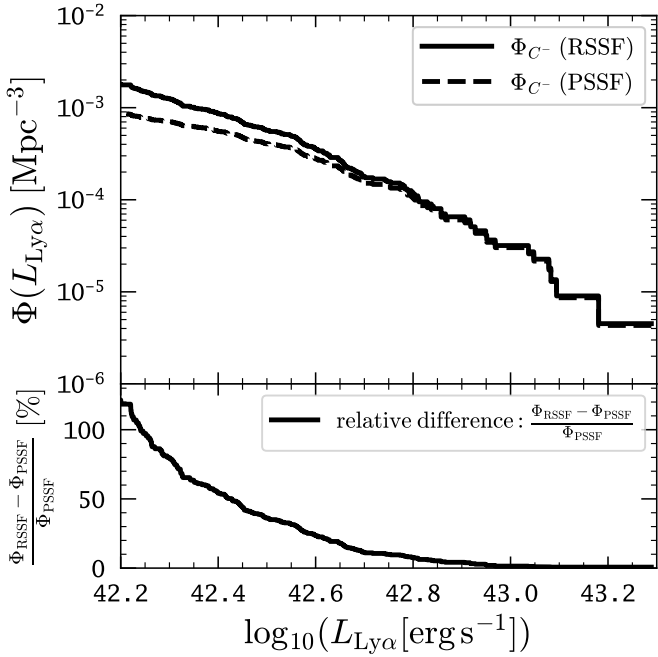


Fig. 9. *Top panel:* global ($2.9 \leq z \leq 6.7$) cumulative LAE LF from MW obtained with the C^- method utilising the RSSF and the PSSF. *Bottom panel:* relative difference (%) between cumulative LFs utilising the RSSF and PSSF.

Numerically, we obtain the same difference between the LAE LFs from the different selection functions when utilising the $1/V_{\text{max}}$ estimator (Sect. 4.1.1). To demonstrate the similarity in the resulting LFs between C^- and $1/V_{\text{max}}$ we compare in Fig. 10 the inferred cumulative LAE LFs from the two estimators. The maximum discrepancy occurs at the faint end of our probed luminosity range. Here $1/V_{\text{max}}$ provides slightly higher LAE densities than C^- : $\Phi_{1/V_{\text{max}}}(\log L_{Ly\alpha} [\text{erg s}^{-1}] = 42.2) = 1.2 \times \Phi_{C^-}(\log L_{Ly\alpha} [\text{erg s}^{-1}] = 42.2)$. The same result is obtained for the PSSF. As outlined in Sect. 4.1.3, while the C^- construction requires only an evaluation of the selection function at redshifts where objects are detected, the $1/V_{\text{max}}$ estimate requires the evaluation of an integral over the selection function at all redshifts. Since our selection function stems from an extrapolation of the results from a source insertion and recovery experiment at five discrete wavelengths, the two estimators deal differently with possible uncertainties from this extrapolation approach. Encouragingly, the differences in the final LAE LF result are small. This validates the robustness of our selection function construction.

Lastly, we compute binned estimates from our sample using the bins motivated in Sect. 4.2 with the $1/V_{\text{max}}$ (Sect. 4.1.1) and ϕ_{PC} (Sect. 4.1.2) estimators. The results are given in Table 2. In Fig. 11 we compare the results from the two different estimators. Following the expectation of Page & Carrera (2000), the binned $1/V_{\text{max}}$ estimator is biased to higher values of the differential LF, especially in the low-luminosity bins near the completeness limit. We find the maximum discrepancy in the lowest luminosity bin to be 8%. However, at the current size of the MW sample the results are within the statistical counting error for each bin. Nevertheless, we encourage the use of the Page & Carrera (2000) estimator in future constructions of the binned LAE LF with larger samples since it is less biased compared to the classical $1/V_{\text{max}}$ techniques in the lowest luminosity bins of the sample (see also Yuan & Wang 2013).

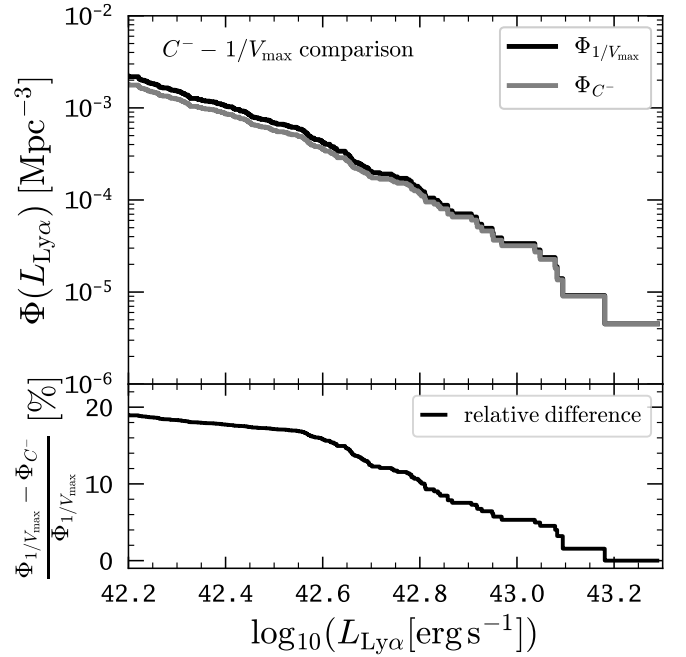


Fig. 10. Comparison of the RSSF completeness corrected cumulative LAE LFs obtained with the C^- and $1/V_{\text{max}}$ estimators. *Top panel:* cumulative LAE LFs from the two methods. *Bottom panel:* relative difference (%) between the $1/V_{\text{max}}$ and C^- methods.

5.2. Parametric modelling

In order to obtain a parametric form of the LAE LF we evaluate the inverted log-likelihood function in Eq. (22) “brute-force” for a densely sampled grid of the Schechter function (Eq. (19)) parameters L^* and α . The minimum of Eq. (22) function represents the maximum-likelihood solution. It is found for $\log L^* [\text{erg s}^{-1}] = 42.66$ and $\alpha = -1.84$. The corresponding value for the normalisation ϕ^* is $\log \phi^* [\text{Mpc}^{-3}] = -2.71$. In Fig. 12 the $\Delta S = 2.3$, and $\Delta S = 6.17$ contours from the evaluation of Eq. (22) are shown. These two contours correspond to the standard 1σ and 2σ confidence regions (68.3% and 95.4%). In this figure we also visualise the dependence of the normalisation ϕ^* on L^* and α .

From the “banana-shaped” appearance of the ΔS contours in Fig. 12 it is evident that we have a strong degeneracy between L^* and α : higher L^* values require steeper faint-end slopes, i.e. smaller α values, and vice-versa. By marginalising over α and L^* we recover the 1D 68.3% confidence intervals $\log L^* [\text{erg s}^{-1}] = 42.66^{+0.22}_{-0.16}$ and $\alpha = -1.84^{+0.42}_{-0.41}$, respectively. These 1D errors are also drawn as error bars around the maximum-likelihood value in Fig. 12. These Schechter parameters are within the 68.3% confidence intervals from the ML analysis performed by Drake et al. (2017b) on the MUSE HUDF data: $\log L^* [\text{erg s}^{-1}] = \{42.72^{+0.23}_{-0.97}, 42.74^{+\infty}_{-0.19}, 42.66^{+\infty}_{-0.19}\}$ and $\alpha = \{-2.03^{+0.76}_{-0.07}, -2.36^{+0.17}_{-\infty}, -2.86^{+0.76}_{-\infty}\}$ for the redshift ranges $2.9 \leq z \leq 4$, $4 < z \leq 5$, and $5 < z \leq 6.64$, respectively. We note that in Drake et al. (2017b) the 1D confidence intervals on L^* and α were estimated by taking the extremes of the $\Delta S = 1$ contour, i.e. without doing the marginalisation. This estimation implicitly assumes a 2D Gaussian distribution for the likelihoods (James 2006). Nevertheless, we verified that the extremes of the $\Delta S = 1$ contour are in good agreement with the marginalised confidence limits, but we caution that such 1D errors do, by construction, not reflect the interdependence between α and L^* . Importantly,

Table 2. Binned differential LAE LF from the first 24 MW pointings.

$\log L_{\text{Ly}\alpha}$ (erg s^{-1})	N_{LAE}	ϕ_{PC} ($\text{Mpc}^{-3}[\Delta \log L_{\text{Ly}\alpha}]^{-1}$)	$\Delta\phi_{\text{PC}}$ ($\text{Mpc}^{-3}[\Delta \log L_{\text{Ly}\alpha}]^{-1}$)	$\phi_{1/V_{\text{max}}}$ ($\text{Mpc}^{-3}[\Delta \log L_{\text{Ly}\alpha}]^{-1}$)	$\Delta\phi_{1/V_{\text{max}}}$ ($\text{Mpc}^{-3}[\Delta \log L_{\text{Ly}\alpha}]^{-1}$)
42.3	52	5.5×10^{-3}	7.7×10^{-4}	5.9×10^{-3}	8.6×10^{-4}
42.5	59	3.0×10^{-3}	4.0×10^{-4}	3.1×10^{-3}	4.1×10^{-4}
42.7	40	1.4×10^{-3}	2.2×10^{-4}	1.4×10^{-3}	2.3×10^{-4}
42.9	17	4.7×10^{-4}	1.1×10^{-4}	4.8×10^{-4}	1.2×10^{-4}
43.1	6	1.4×10^{-4}	5.8×10^{-5}	1.5×10^{-4}	5.9×10^{-5}
43.3	1	2.3×10^{-5}	2.3×10^{-5}	2.3×10^{-5}	2.3×10^{-5}

Notes. ϕ_{PC} is computed with the Page & Carrera (2000) estimator (Sect. 4.1.2), while $\phi_{1/V_{\text{max}}}$ results from the binned $1/V_{\text{max}}$ estimator (Sect. 4.1.1).

this interdependence needs to be taken into account when discussing the LAE LF redshift evolution based on parametric LF fits¹⁴.

In Fig. 13 we compare the maximum-likelihood estimated Schechter function LF to the non-parametric $1/V_{\text{max}}$ estimate. The in this figure shown 68.3% and 95.5% confidence limits on the cumulative Schechter function were obtained by randomly drawing¹⁵ 1000 LAE LFs from the normalised likelihood function (Eq. (20)). We deliberately compare here the parametric results to the non-parametric $1/V_{\text{max}}$ estimate, because in both approaches the selection function needs to be integrated over the whole redshift range (compare denominators in Eq. (21) and Eq. (7)), which is not the case for the C^- method. Thus, a comparison of the maximum-likelihood results to the C^- results would stand on unequal footing. As evident from Fig. 13, there is excellent agreement between the non-parametric and parametric LFs, indicating that indeed the Schechter parameterisation appears qualitatively to be a valid description of the LAE LF.

We also test whether a power law (Eq. (23)) is a more suitable parameterisation of the LAE LF from our MW data. To this end, we first calculate the inverted log-likelihood function for a fine sampled grid of power-law slopes β . We find the minimum in S at $\beta = -2.99 \pm 0.12$. The normalisation, evaluated at $\log L^* = 42.5$, is $\log \phi^* = -2.932 \pm 0.006$. We also perform the same analysis without excluding the AGN from the sample. In this case we recover a slope $\beta = -2.94 \pm 0.12$ and normalisation $\log \phi^* = -2.930 \pm 0.006$ (at $\log L^* = 42.5$).

Equipped with these results, we now quantify the goodness of fit. Our statistical analysis will enable us to decide whether the power-law or Schechter parameterisation describes the LAE LF more adequately. A possible statistical test in this respect is the Kuiper test (e.g. Press et al. 1992; Ivezić et al. 2014). This test bears similarities to the well-established Kolmogorov-Smirnov (KS) test, but it is more sensitive to the discrepancies in the wings of the distribution (see also Wisotzki 1998). Hence, it is more suitable for the situation at hand as the exponential cut-off to the power law in the Schechter function modulates the expected frequency of the brighter galaxies in our probed luminosity range. Nevertheless, for comparison purposes we also compute the classical KS tests. Both tests are one-dimensional, thus require marginalisation over our sample and the model distributions (explained below), either over redshifts or luminosities. When marginalising over redshifts we thus test for discrepancies between the observed and model luminosity

¹⁴ To facilitate this discussion in future work, we release our obtained $S(\log L_{\text{Ly}\alpha}, \alpha)$ and $\phi^*(\log L_{\text{Ly}\alpha}, \alpha)$ functions shown in Fig. 12 with this publication via the CDS.

¹⁵ Random draws were realised with the rejection method (Press et al. 1992).

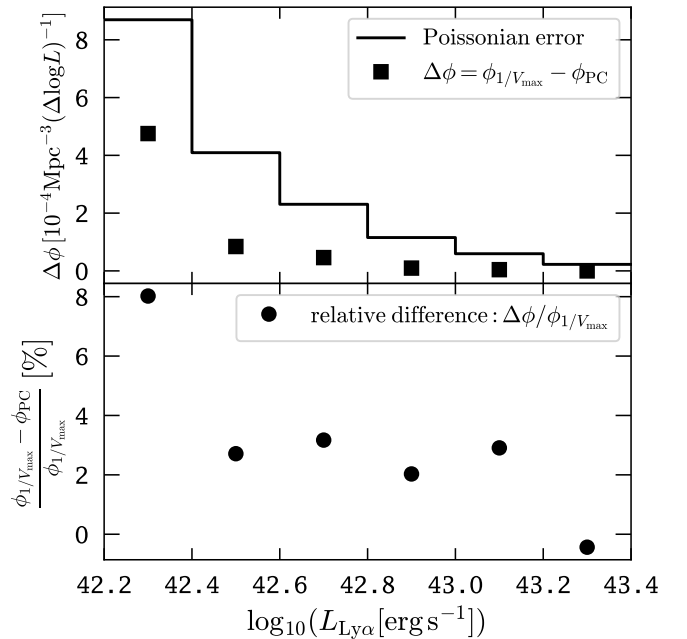


Fig. 11. Top panel: absolute difference between binned $1/V_{\text{max}}$ and ϕ_{PC} estimator for global MW LAE LF in comparison to the Poissonian errors in each bin. Bottom panel: relative difference (%) between the two binned estimators.

distributions. Given the assumption of a non-evolving LF over the probed redshifts, which was already backed with evidence in the previous section, this marginalisation provides the most powerful metric for testing the different LF parameterisations. Marginalising over luminosities, on the other hand, tests whether the observed distributions in redshifts are adequately described by one parameterisation. This provides us with a parametric test for redshift evolution. Finally, dealing with a 2D distribution in redshift-luminosity space we also calculate a 2D variant of the KS statistic that was originally developed by Peacock (1983).

A possible pitfall when utilising these tests is that we determined the model parameters from the same dataset. As explained in Wisotzki (1998), the distribution functions of these test statistics are thus not valid anymore for calculating the p -values needed to reject or accept the null hypothesis that the “data is represented by the model”. This is because the null hypothesis model has been moved closer to the data due to its estimation from the data. We circumvent this by performing Monte Carlo simulations to calculate the distribution of these test statistics under the null hypothesis (Chap. 14.3, Press et al. 1992). Therefore, we draw a large number of samples of the same size as

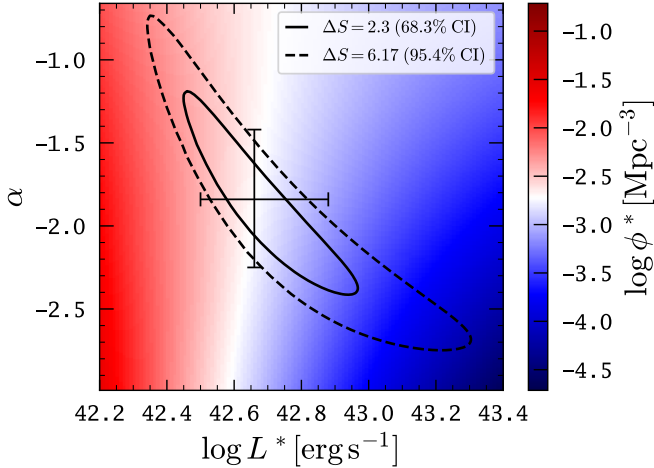


Fig. 12. Results from the Schechter function ML fit for the global MW LAE LF. Contours are drawn at $\Delta S = \{2.3, 6.17\}$ thereby outlining the {68.3%, 95.4%} confidence intervals for α and $\log L^*$. In colour we show the normalisation $\log \phi^*$, which is a dependent quantity on α and L^* , i.e. it is not a free parameter in the fitting procedure. The cross indicates the best-fitting $(\log L^*[\text{erg s}^{-1}], \alpha) = (42.66, -1.84)$. At this point in $\log L^* - \alpha$ space the dependent normalisation is $\log \phi^*(\log L^*, \alpha)[\text{Mpc}^{-3}] = -2.71$. The 1D error bars show the 68.3% confidence interval from the marginalised distribution in α and $\log L^*$ (see text).

our LAE LF sample from the ML luminosity function models. In these simulations we account for the surveyed area, the MW selection function (RSSF), and the $f_c = 0.15$ sample truncation criterion. We show in Fig. 14 the resulting 2D distributions in redshift-luminosity space from the maximum-likelihood models together with the MW LAE sample. Moreover, we also show in this figure the marginalised differential and cumulative distributions in redshift- or luminosity-space, together with binned histograms of the actual samples for the Schechter function, for the power law, and for the power law without exclusion of the two AGN in the sample. The 2D KS test-statistics are computed by comparing the 2D model distributions to the actual samples, and the 1D KS- and Kuiper-tests are computed by comparing the cumulative 1D model distributions to the cumulative sample distribution. We list in Table 3 the resulting p -values from those tests.

It is already visually apparent, especially when contrasting the panels comparing the cumulative distributions in $L_{Ly\alpha}$ in Fig. 14, that the expected distributions from the power-law parameterisations show marked discrepancies with respect to the observed distribution. This visual impression is confirmed by the p -values (Table 3). All three statistical tests result in markedly smaller p -values for the power-law model compared to those for the Schechter model. The KS- and Kuiper-tests in redshift space result in p -values for which neither the power-law model nor the Schechter model can be formally rejected. This shows that a single parameterisation of the LAE LF is adequate to describe the LAE LF over the redshift and luminosity range probed by MW, but the Schechter model can be favoured due to its markedly higher p -values. This result is consistent with the non-parametric test presented in the previous section that indicated a non-evolving LAE LF over the redshift range probed by MW (Table 1). Given the non-evolving LF, the resulting $p = 0.04$ of the Kuiper test in $L_{Ly\alpha}$ for the power-law model means that we can reject this parameterisation at 2σ significance. Only when not excluding the X-ray identified AGN from the LAE sample, the power law becomes a marginally consistent

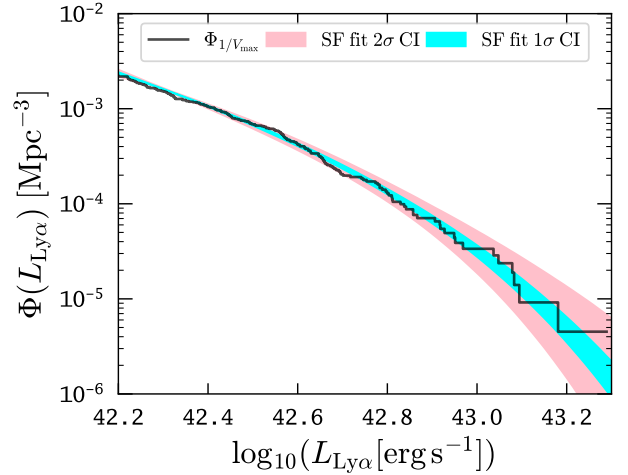


Fig. 13. Cumulative LAE LF from MW obtained with the $1/V_{\text{max}}$ estimator in comparison to 68.3% and 95.4% confidence limits of the ML Schechter fit.

description of the sample. Based on these results we adopt our ML Schechter model as the working hypothesis for the remainder of this paper.

We note that parametric models for LAE LFs in the literature are sometimes obtained by χ^2 fitting a model to non-parametric binned estimates of the differential LF (e.g. van Breukelen et al. 2005; Cassata et al. 2011; Matthee et al. 2015; Santos et al. 2016). However, we caution that the resulting model parameters and uncertainties depend on the placement and width of the bins. We visualise this for our sample in Fig. 15. There we show the resulting (L^*, α) values from a non-linear fit (obtained with the Levenberg-Marquardt algorithm) of the Schechter function (Eq. (19)) to different binned $1/V_{\text{max}}$ estimates (Eq. (8)). For this exercise we varied both the size (different panels in Fig. 15) and the placement (different colours in Fig. 15) of the bins. Moreover, we ignored incomplete bins, i.e. bins with objects that fall below the $f_c = 0.15$ truncation criterion, in the fitting procedure. As is evident, the resulting (L^*, α) pairs scatter substantially, with only a few combinations of bin-width and bin-placement reproducing the actual ML solution. Thus, this fitting approach will not lead to a robust parameterisation of the LF. However, given a ML solution it could potentially be used to determine an optimal bin-width and bin-placement at which the binned estimate will be closest to the adopted parametric form. Indeed, for our adopted bin-width ($\Delta \log L_{Ly\alpha}[\text{erg s}^{-1}] = 0.2$) and bin-placement (lowest luminosity boundary $\log L_{Ly\alpha}[\text{erg s}^{-1}] = 42.2$), the parametric fit to the binned data is in very good agreement with the ML solution.

We plot in Fig. 16 the non-parametric differential MW LAE LF in three redshift bins ($2.9 < z \leq 4$, $4 < z \leq 5$, and $5 < z \leq 6.7$), as well as the global ($2.9 < z < 6.7$) LAE LF. The non-parametric results shown in this figure are obtained with the ϕ_{PC} method for the RSSF and the PSSF. For both the redshift bins and the whole redshift range we also display the 68.3% and 95.4% confidence intervals of the global Schechter LF. As for Fig. 13, these intervals were obtained by randomly drawing 1000 LAE LFs from the normalised likelihood function. Here it can be seen that the global Schechter fit is an excellent description of the global binned RSSF LF. This result confirms what we saw already when comparing the parametric to the non-parametric cumulative LAE LFs in Fig. 13. Moreover, the binned estimates in the different redshift bins are also in excellent agreement with the global Schechter parameterisation,

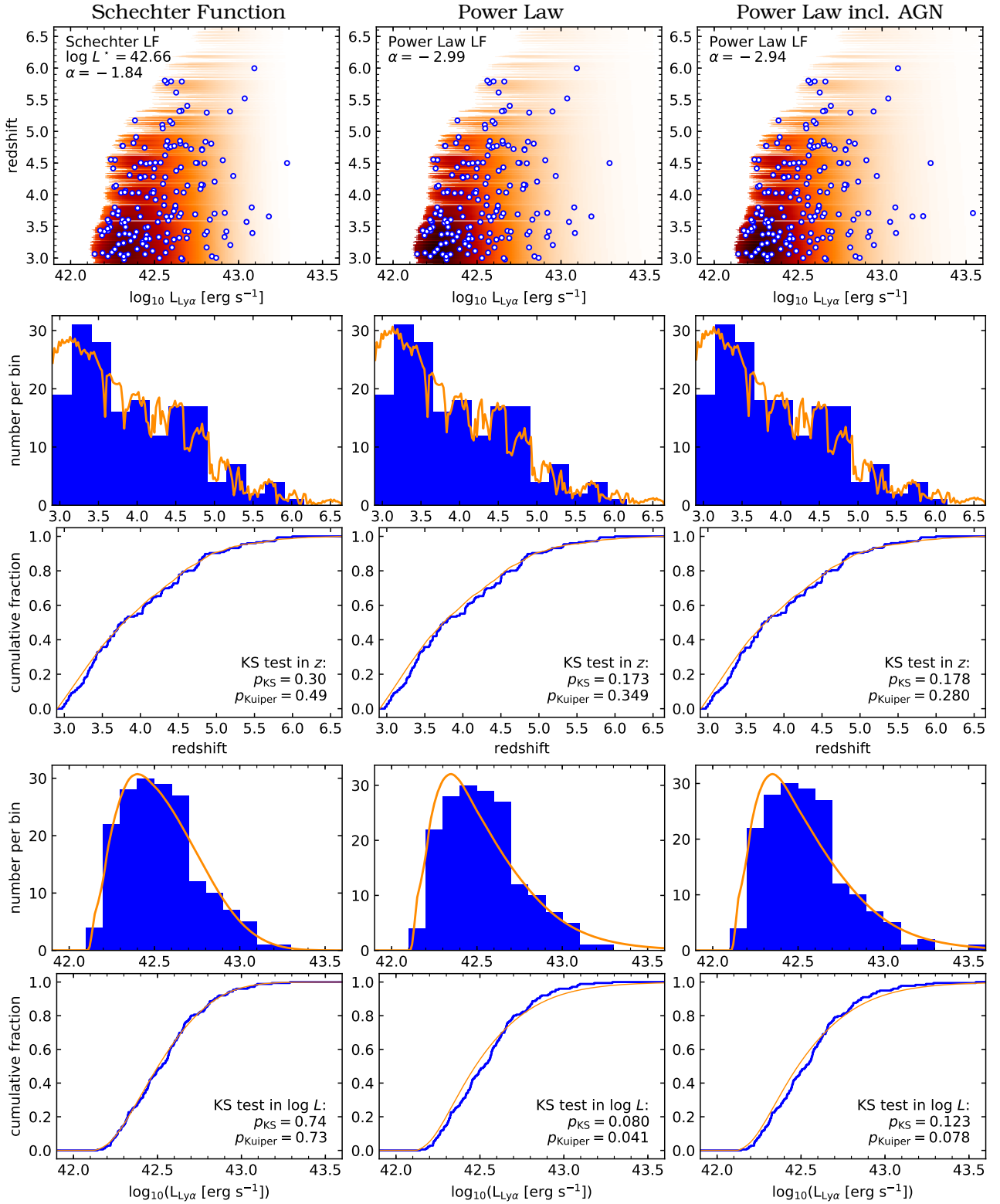


Fig. 14. Visualisation of the procedure to calculate the Kuiper- and KS-test statistics for the Schechter model (*left panels*), power-law model (*centre panels*), and the power-law model fit to the LAE sample where the X-Ray identified AGN were not excluded (*right panels*). The panels in the *first row* show the expected LAE distribution in redshift-luminosity space from the best-fit parameterisations folded with the MW survey area, selection function, and $f_c = 0.15$ truncation criterion in shaded orange, while blue circles show the actual LAE samples in redshift-luminosity space. The 2D KS-test statistic is computed by comparing the actual samples to the model distributions. The panels in the *second row* show predicted number counts computed from the distributions in the first row as a function of redshift in comparison to a histogram of the observed number counts (blue histogram). In the *third row* we show the comparison between the normalised cumulative distribution in redshift (blue line) and the cumulative distribution from the model (orange line). These curves are used to calculate the Kuiper and 1D KS-test in redshift. The panels in the *fourth and fifth row* are similar to those in the second and third row, respectively, but compare the differential and cumulative distribution in $L_{Ly\alpha}$ -space to the model distributions.

Table 3. p -values from Monte Carlo calibrated KS and Kuiper tests of the observed distribution against maximum-likelihood LF models obtained by folding the maximum-likelihood Schechter (Eq. (19)) or power-law (Eq. (23)) parameterisations with the MW survey area and LAE selection function (RSSF), as well as the $f_c = 0.15$ truncation criterion.

Parameterisation	$P_{\text{KS}}^{L_{\text{Ly}\alpha}}$	$P_{\text{Kuiper}}^{L_{\text{Ly}\alpha}}$	P_{KS}^z	P_{Kuiper}^z	$P_{2\text{DKS}}$
Schechter ($\log L^* = 42.66$, $\alpha = -1.84$, $\log \phi^* = -2.71$)	0.74	0.73	0.30	0.49	0.87
Power Law ($\log L^* = 42.5$, $\beta = -2.99$, $\log \phi^* = -2.932$)	0.08	0.04	0.17	0.35	0.23
Power Law incl. AGN ($\log L^* = 42.5$, $\beta = -2.94$, $\log \phi^* = -2.930$)	0.12	0.08	0.18	0.29	0.30

Notes. One-dimensional KS and Kuiper tests are performed in redshift and luminosities, while the 2D KS test operates directly in redshift-luminosity space (see Fig. 14). L^* in erg s^{-1} and ϕ^* in Mpc^{-3} .

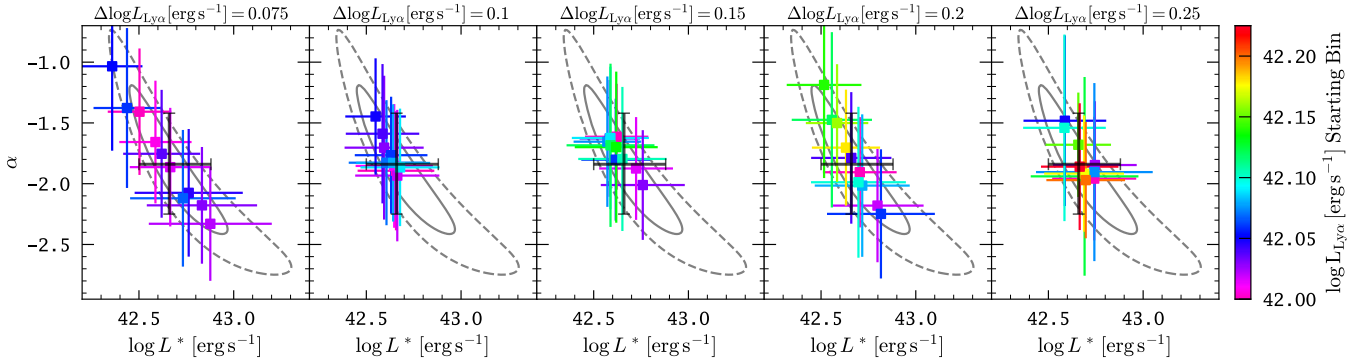


Fig. 15. Resulting Schechter parameters L^* and α from a non-linear least-squares fit (using the Levenberg-Marquardt algorithm) of the Schechter function (Eq. (19)) to the binned differential $1/V_{\text{max}}$ estimator (Eq. (8)) for different binning schemes. Panels from left to right show five different bin sizes $\Delta \log L_{\text{Ly}\alpha} [\text{erg s}^{-1}] = \{0.075, 0.1, 0.15, 0.2, 0.25\}$. Colour-coded in each panel is the best-fit (L^* , α) pair according to the lowest-luminosity boundary of the starting bin. Incomplete bins (containing objects at $f_c < 0.15$) are ignored in the fit, i.e. the magenta point in the panel $\Delta \log L_{\text{Ly}\alpha} [\text{erg s}^{-1}] = 0.2$ panel represents the adopted binning scheme (see Sect. 4.2) in Table 2 and Fig. 17. For guidance the likelihood contours and the maximum-likelihood solution from Fig. 12 are shown in each panel.

thus adding further evidence to our previous tests that indicated a non-evolving apparent LAE LF. All these results justify the use of a global LAE LF in this redshift range by MW. Hence, the estimates in the redshift bins here serve only demonstrative purposes and will not be considered further. For the same reason, parametric estimates in the redshift bins are prohibitive for our sample as they just would lead to a larger uncertainty on the final fitting parameters (known as overfitting). We have commented already on the upward correction of the LAE LF by up to a factor of 2.5 at the faint end of our probed luminosity range when utilising the RSSF instead of the PSSF (Sect. 5.1). Finally, in the comparison between RSSF and PSSF corrected LFs presented here, it can be seen that neglecting extended Ly α emission in the selection function naturally leads to the inference of a flatter faint-end slope α in the Schechter parameterisation. We demonstrate in the next section that the PSSF corrected values are in better agreement with previously determined literature estimates.

We also compare in Fig. 16 the MW LAE LF to published LAE LF estimates from other MUSE surveys performed within the MUSE consortium (Bina et al. 2016; Drake et al. 2017b,a). Key parameters from these surveys are also listed in Table 4. Both the binned estimates from the pilot study by Bina et al. (2016), which makes use of the lensing cluster Abell 1689, as well as the global LAE LF determination from the deep MUSE commissioning data in the *Hubble* Deep Field South show some agreement at the 1σ level with our estimates. However, the error bars from these early analyses of MUSE data are quite large, and the estimates scatter substantially. More relevant is the good agreement between our results and the binned estimates from the MUSE-Deep programme in the *Hubble* Ultra

Deep Field by Drake et al. (2017b). Where the luminosity ranges between MUSE-Deep and the MW sample presented here overlap, the data points are in almost perfect agreement, except for the brightest Drake et al. (2017b) bins for the redshift range $2.9 < z \leq 4$ and for the global LF. However, the mismatch in those brightest bins is a consequence of the pencil-beam nature of the MUSE Deep survey, making it prone to cosmic variance for such brighter and rarer LAEs. We again note that the Drake et al. (2017b) study also incorporates a correction for extended Ly α halos in their completeness function estimates. In this respect it is especially encouraging that even their faintest bins ($\log L_{\text{Ly}\alpha} [\text{erg s}^{-1}] < 42.0$) are in agreement with the 2σ contours of our extrapolated Schechter parameterisation below the luminosity limit of MW¹⁶, except at $z > 5$. There, however, the faintest bins are below the adopted $f_c = 0.25$ completeness cut-off for the parametric modelling in Drake et al. (2017b) as at these low completeness levels the selection function was deemed unreliable. The comparison with the MUSE-deep analyses demonstrates how MW is complementary at brighter luminosities. In a forthcoming study we will perform a joint and homogenised LAE LF analysis of the deep and wide MUSE datasets.

6. Comparison with the literature

We now compare the obtained MW LAE LF with previous literature estimates in the redshift range $3 \lesssim z \lesssim 6$. For this purpose

¹⁶ As discussed in Drake et al. (2017b), their faintest bins at $3 < z < 4$ are consistent with the LAE LF construction at $z \sim 3$ from a blind 92 h long-slit integration with FORS2 by Rauch et al. (2008).

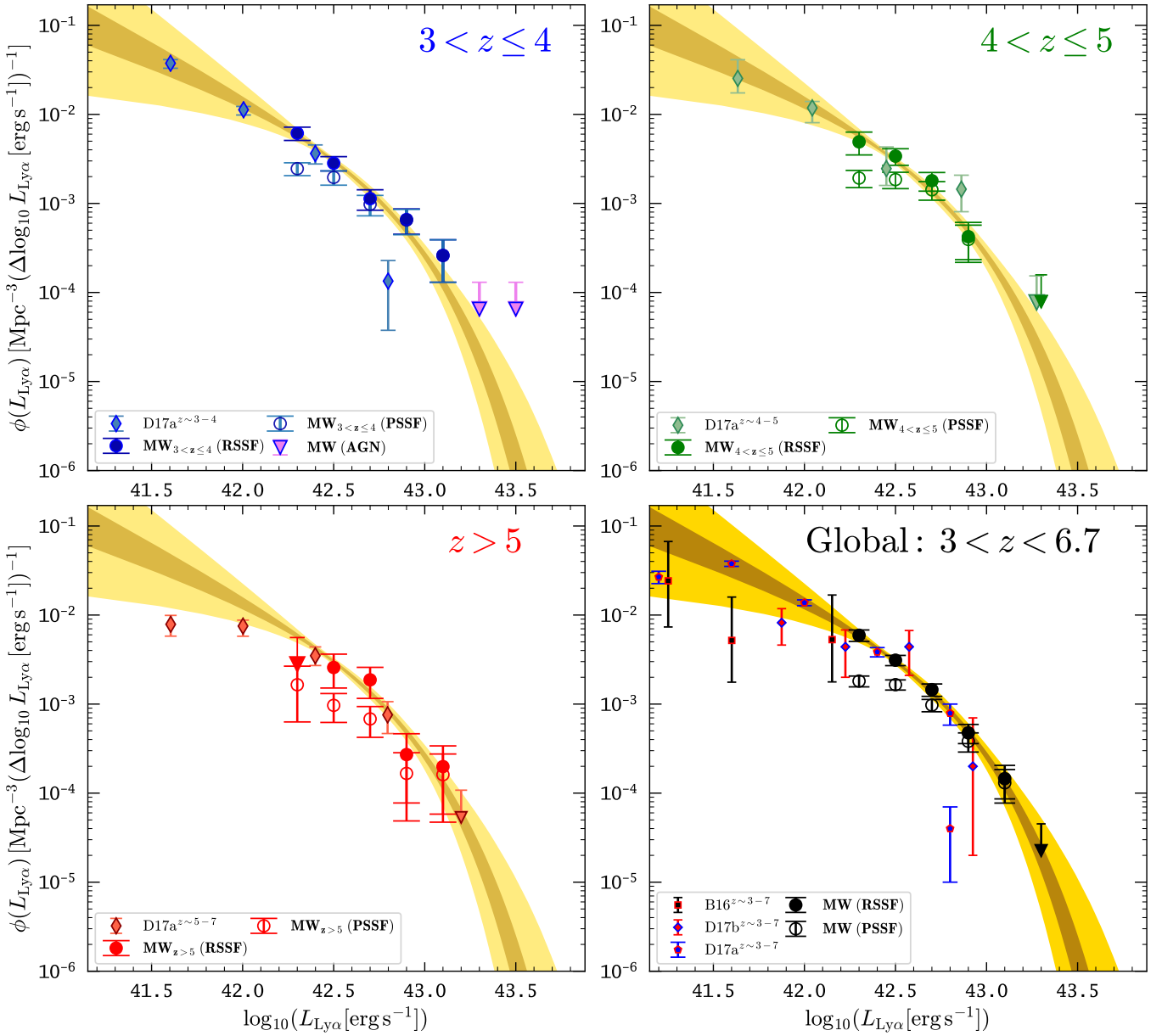


Fig. 16. Differential MUSE-Wide LAE LF in the redshift ranges $2.9 < z \leq 4$ (top left), $4 < z \leq 5$ (top right), $5 < z < 6.7$ (bottom left), and for the global MW redshift range (bottom right). Our RSSF (see Sect. 3.2) corrected binned estimates are shown as filled circles, while with the oversimplified PSSF (see Sect. 3.1) corrected binned estimates are shown with open circles. Yellow (dark yellow) shaded regions indicate the 68.3% (95.4%) confidence regions for a Schechter parameterisation obtained a maximum likelihood analysis (Sect. 4.3). For this parametric modelling we corrected with the RSSF for completeness. Also shown in this figure are other MUSE LAE estimates obtained by the MUSE GTO consortium, namely the binned estimates by Drake et al. (2017a) obtained from MUSE commissioning observations in the *Hubble* Deep Field South, the binned estimates by Drake et al. (2017b) from the MUSE-Deep observations in the *Hubble* Ultra Deep Field, and the pilot study by Bina et al. (2016) exploiting gravitational lensing by the lensing cluster Abell 1689.

we utilise the literature compilation of binned differential LAE LF estimates provided by Sobral et al. (2018a), with the exception of a few references which were not present in that compilation (namely the studies by Shimasaku et al. 2006; Shioya et al. 2009; Henry et al. 2012¹⁷; and Konno et al. 2018). An overview of the comparison studies is provided in Table 4, where we list their methodology, redshift ranges, survey areas, probed comoving volumes, as well as the lowest Ly α luminosities to which the LAE LF was probed. For the imaging campaigns we also

list the adopted equivalent width cuts, as well as the number of photometric LAE candidates and actual spectroscopic confirmations.

Except for the MUSE studies mentioned at the end of the previous section only Sobral et al. (2018a) attempted to construct a global LAE LF over a similar redshift range. We provide a comparison between their binned estimates and our binned and parametric estimates in Fig. 17. Where the MW luminosity range overlaps with SC4K, the two LF estimates are in agreement, except for the faintest SC4K bins. These bins fall below our RSSF corrected results and line up more closely with our PSSF corrected binned estimates. We comment on this mismatch at the

¹⁷ We use the “inferred LAEs, high LF” estimate from Henry et al. (2012), for which the less certain LAEs were also kept in the sample.

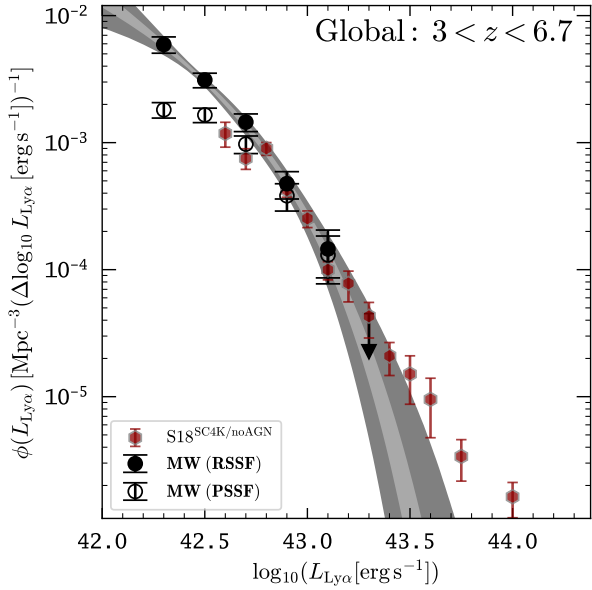


Fig. 17. Global ($2.9 \leq z \leq 6$) MUSE-Wide LAE LF (binned RSSF and PSSF corrected results from filled and open circles, respectively) with 1σ (dark grey shaded region) and 2σ intervals (light grey shaded region) for the RSSF corrected Schechter parameterisation as in the bottom right panel of Fig. 16, in comparison to the binned estimates of the global ($2.5 \leq z \leq 6$) SC4K LAE LF (Sobral et al. 2018a).

of a galaxy compared to its overall ionising photon production, which as a good first-order approximation can be traced by its UV luminosity (e.g. Bouwens et al. 2016; Schaerer et al. 2016). In principle the UV and LAE LFs can be linked to each other (Henry et al. 2012; Gronke et al. 2015). However, in which way radiative transfer processes or additional Ly α photon production processes (e.g. ionising photons from UV undetected satellite galaxies or Ly α boosting from the UV background as proposed in Mas-Ribas & Dijkstra 2016) could influence the bright end of the LAE LF compared to the bright end of the UV LF remains currently purely speculative. A few of the most-luminous LAES at $z \gtrsim 6$ have already received observational attention (e.g. Ouchi et al. 2009; Lidman et al. 2012; Hu et al. 2016; Matthee et al. 2018), with one object being suggested to either host metal-free stars (Sobral et al. 2015) or a direct-collapse black hole (Pallottini et al. 2015). At $z \sim 2-3$ Sobral et al. (2018b) presented recently spectroscopic results on 20 bright LAEs ($\log L_{\text{Ly}\alpha} [\text{erg s}^{-1}] > 42.7$). Interestingly, these authors report a 60% AGN fraction for such luminous LAEs, which rises sharply to 100% for $\log L_{\text{Ly}\alpha} [\text{erg s}^{-1}] > 43.3$. This indeed suggests that the observed deviations from a Schechter function at bright luminosities are caused by sources whose Ly α emission is powered by non-thermal black hole accretion processes rather than star formation.

We also find some notable overall disagreements between the literature and our estimates in luminosity range where MW overlaps with other surveys. In the redshift range $2.9 < z \leq 4$ (top left panel in Fig. 18) we find that our LF is significantly higher (up to an order of magnitude) than the LF estimates obtained by Cassata et al. (2011). However, the Cassata et al. $z \sim 3-4$ LF is also significantly below most other literature estimates and it is only consistent with the faint end ($\log L_{\text{Ly}\alpha} [\text{erg s}^{-1}] \leq 42.5$) of the Grove et al. (2009) LF. Moreover, most of the LF bins from Dawson et al. (2007) $z \sim 4$ (centre panel in Fig. 18) are significant below our inferred LF.

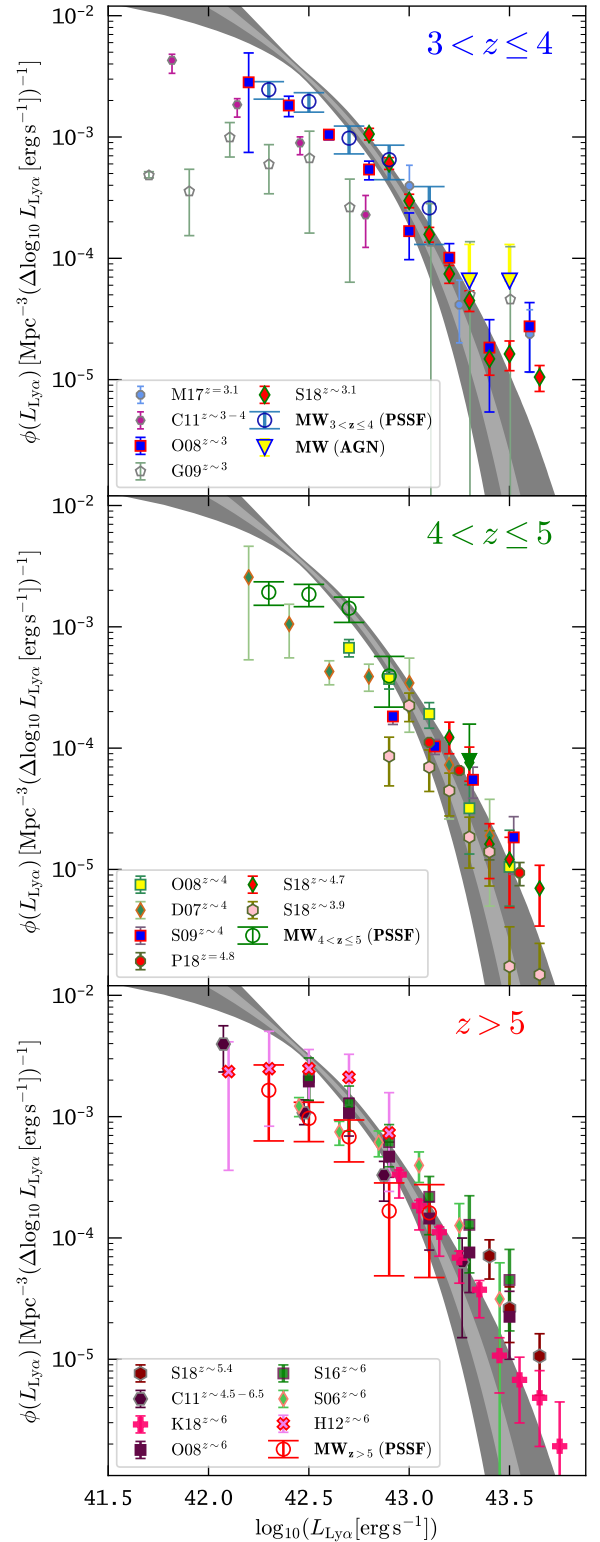


Fig. 18. Differential LAE LF estimates from the literature grouped in three redshift bins ($2.9 < z \leq 4$ in the top panel, $4 < z \leq 5$ in the middle panel, and $5 < z \leq 6$ in the bottom panel) compared to our 1σ (dark grey shaded region) and 2σ intervals (light grey shaded region) for the RSSF corrected global Schechter parameterisation (shown already in Figs. 16 and 17). References are provided in Table 4; in the legend we abbreviate with the first letter of the first author and the last two digits of publication year. We also show our PSSF corrected binned estimates as open circles, as they are often in better agreement with the literature estimates (see text).

Finally, we find from the comparison in Fig. 18, where we group the literature results in three redshift bins that the majority of literature LF estimates at luminosities $\log L_{\text{Ly}\alpha} \lesssim 42.5$ fall below our global Schechter parameterisation. We note again that this parameterisation was obtained by implicitly correcting for extended low surface brightness Ly α halos by utilising our RSSF. In this respect it is especially interesting that the majority of the literature estimates are often in nearly perfect agreement with our PSSF completeness corrected LF estimates. Especially the binned estimates of Ouchi et al. (2008) at $z \sim 3$, as well as the binned estimate from Shimasaku et al. (2006) and Cassata et al. (2011) at $z \sim 6$ line up perfectly with our PSSF corrected estimates. Thus, we are able to reproduce the results of previous campaigns by using a completeness correction that is comparable to the ones applied in those studies.

Notably, almost all LAE LF estimates in the literature to date have not taken the extended nature of LAEs into account when constructing their selection functions. For example, Ouchi et al. (2008) populate their NB imaging data with fake point sources, while Hao et al. (2018), at $z \sim 2$, rescale the flux of stellar images in their images. A slightly different approach was used by Konno et al. (2018) who utilise a Sèrsic $n = 1.5$ surface-brightness profile with small effective radii of $r_e = 0.9$ kpc, but these fake sources also do not correctly represent the typical extended Ly α surface-brightness profiles. As the source detection algorithms used in these surveys utilise parameters optimised for the detection of compact sources, we argue that the inferred selection functions in these studies must be too optimistic. As we elaborate later, this leads to a bias in the luminosity function estimate near the completeness limit of the surveys, thus leading to incorrect estimates at the faint end of the LAE LF. Moreover, the faint-end studies at $z \sim 6.5$ appear to be in subtle disagreement (Ouchi et al. 2010; Matthee et al. 2015). Interestingly, Matthee et al. (2015) followed a different approach to Ouchi et al. (2010) to estimate their completeness by rescaling fluxes of other sources in the NB filter that do not show an excess but otherwise fulfil the additional colour-selection criteria. Nevertheless, this model-independent approach, also utilised in Sobral et al. (2018a), neglects that a significant fraction of Ly α emission comes from the diffuse low-SB halo.

We argue here that assuming LAEs to be compact point-like sources is no longer a justifiable simplification. As already mentioned in Sect. 5.1, Grove et al. (2009) suspected an inherent bias in LAE LF estimates caused by ignoring possible extended emission in the construction of the selection function. Moreover, the LAEs found in the deep long-slit integration of Rauch et al. (2008), and those in the stacking analyses by Steidel et al. (2011) and Momose et al. (2014), already hinted at a large fraction of LAEs being surrounded by low surface brightness Ly α halos. Now, from the MUSE deep fields, the omnipresence of Ly α halos around LAEs is a well-established fact on an object-by-object basis (Wisotzki et al. 2016; Leclercq et al. 2017). Here we show that accounting for this effect results in an upward correction by a factor of up to three for LF bins at $\log L_{\text{Ly}\alpha} [\text{erg s}^{-1}] \lesssim 42.5$ of previous surveys.

7. Summary and outlook

We presented a framework for constructing the LAE LF in an integral field spectroscopic survey. We utilised these methods on the LAE sample resulting from the first instalment of the MW survey. Our LAE LF sample covers luminosities $42.2 \leq \log L_{\text{Ly}\alpha} [\text{erg s}^{-1}] \leq 43.5$. We show that the apparent LAE LF

in this luminosity range is non-evolving over the redshift range $2.9 \leq z \leq 6.7$. This result is irrespective of the assumed selection function, but we argued that the classical assumption of LAEs being compact-point like objects biases LF estimates too low near the completeness limit of a survey. We found that different non-parametric estimates provide nearly identical descriptions of the cumulative or differential LAE LF. We obtained a maximum-likelihood Schechter parameterisation of the LAE LF for $\log L^* [\text{erg s}^{-1}] = 42.66^{+0.22}_{-0.16}$, and $\alpha = -1.84^{+0.42}_{-0.42}$, but with a strong degeneracy between the two parameters. The posterior normalisation of the maximum-likelihood Schechter fit is $\log \phi^* [\text{Mpc}^{-3}] = -2.71$. We show that the Schechter parameterisation accurately describes our non-parametric cumulative and differential estimates, while parametrising the LAE LF with a simple power law provides a less optimal fit. A comparison of our LAE LF with binned estimates of the differential estimates from the literature revealed subtle disagreements. Especially at fainter luminosities ($\log L_{\text{Ly}\alpha} [\text{erg s}^{-1}] \lesssim 42.5$), our LF and the Drake et al. (2017b) MUSE HUDF LAE LF are higher than the literature LF estimates. This is a natural consequence of incorporating the dilution of detectable Ly α signal due to extended low surface brightness Ly α halos into the completeness correction. We show that we achieve a better agreement with the literature when assuming for the completeness correction that LAEs are compact point-like sources. However, in light of the recently accumulated evidence regarding the ubiquity of extended Ly α halos, we argued that this is an oversimplified assumption.

With the release of the full MW dataset we will significantly improve the statistical robustness of the results presented here by a factor of more than five, due to the increased sample size. The main drawbacks of the current data are the lack of a sizeable sample of $z > 5$ LAEs and the small number of very luminous ($\log L_{\text{Ly}\alpha} [\text{erg s}^{-1}] > 43.0$) LAEs. Even so, it is especially this currently undersampled region in the $(L_{\text{Ly}\alpha}, z)$ -parameter space where other campaigns hint at a possible evolution in the shape and normalisation of the LAE LF (e.g. Santos et al. 2016; Sobral et al. 2018a). While a robust determination of the bright end of the LAE LF will only be possible within wide-area NB campaigns, MW nicely populates the Ly α luminosity range that overlaps with the faintest ends of such campaigns and the bright ends of the deep MUSE surveys. The next step in our analysis will be the construction of a combined LAE LF from the final MW dataset and the MUSE deep fields.

Of course, with an increased sample size on the horizon, we need to be aware of possible systematic uncertainties in the framework presented here. Firstly, all the non-parametric and parametric LF estimators applied here do not take photometric uncertainties into account. Secondly, we do not account for uncertainties in the selection function.

Regarding the selection function construction we assumed that the ten LAEs from the source insertion and recovery experiment in the HDFS are representative of the whole population, and thus we weighted them equally. We can justify this approach, as no scaling relations between Ly α halo flux fraction and other physical properties have been found. In particular, the halo-flux fraction appears to be independent of Ly α luminosity (Leclercq et al. 2017). And, as we explained in Sect. 3.2, the sources used span a range of halo flux fractions and line profiles. Nevertheless, to date because of selection effects, we do not have a corrected distribution of the halo flux fractions. Equipped with such a distribution in the future, a more realistic weighting scheme could be employed.

However, a more relevant systematic effect might result from ignoring the statistical errors on the flux measurement in the

LF construction. It is known, especially near the completeness limit of a survey where the photometric uncertainties become larger, that ignoring photometric errors systematically biases the LF. This bias is referred to as the Eddington-Malmquist bias in the literature (see e.g. Sect. 5.5 in Ivezic et al. 2014). The bias is a combined effect of photometric errors, sample truncation on observed values, and a rising luminosity function towards fainter luminosities. The effect is that near the completeness limit there are more sources that scatter into the sample than sources that scatter out of the sample. Ultimately this results in higher inferred number source densities at the faint end of the probed luminosity range, and thus also biases the inferred slopes steeper in parametric LF determinations. We point out that our sample truncation was quite conservative (Sect. 4.2), i.e. we excluded almost 1/4 of the faintest sources from our final LAE LF sample. Moreover, in the binned estimates the bin-size was chosen to be larger than the photometric error in the faintest bin, and the sources scattering between the two faintest appear to compensate each other in both directions. A more quantitative discussion is beyond the scope of this analysis, but we note that the Eddington-Malmquist bias has not been commented upon in the LAE LF literature. We argue that robust determinations of the faint-end slope need to account for this bias in the future, for example by modelling the dependence of the photometric uncertainties on the inferred LFs. Of interest in this respect appears the modified ML estimator developed by Mehta et al. (2015) that can account for photometric uncertainties. Methods like this will allow for a robust and unbiased determination of LAE LFs in the future, from which vital information regarding cosmology and galaxy formation can in turn be extracted (see e.g. Bouwens 2016 and Dayal & Ferrara 2018 for recent reviews).

Acknowledgements. We thank the support staff at ESOs VLT for help with the visitor mode observations during GTO. This research made extensive use of the *astropy* package (Astropy Collaboration et al. 2013). All plots in this paper were created using *matplotlib* (Hunter 2007). E.C.H. R.S., T.U., and L.W. acknowledge funding from the Competitive Fund of the Leibniz Association through grants SAW-2013-AIP-4 and SAW-2015-AIP-2. E.C.H. dedicates this paper to Melli's kittens Mary and Jamie.

References

- Adams, J. J., Blanc, G. A., Hill, G. J., et al. 2011, *ApJS*, 192, 5
- Ajiki, M., Taniguchi, Y., Fujita, S. S., et al. 2004, *PASJ*, 56, 597
- Astropy Collaboration (Robitaille, T. P., et al.) 2013, *A&A*, 558, A33
- Bacon, R., Bauer, S. M., Bower, R., et al. 2004, in *SPIE Conf. Ser.*, eds. A. F. M. Moorwood, & M. Iye, 5492, 1145
- Bacon, R., Vernet, J., Borisiva, E., et al. 2014, *The Messenger*, 157, 13
- Bacon, R., Brinchmann, J., Richard, J., et al. 2015, *A&A*, 575, A75
- Bacon, R., Conseil, S., Mary, D., et al. 2017, *A&A*, 608, A1
- Bacon, R., & Monnet, G. J. 2017, *Optical 3D-Spectroscopy for Astronomy* (Weinheim: Wiley-VCH Verlag GmbH & Co. KGaA)
- Bagley, M. B., Scarlata, C., Henry, A., et al. 2017, *ApJ*, 837, 11
- Beckwith, S. V. W., Stiavelli, M., Koekemoer, A. M., et al. 2006, *AJ*, 132, 1729
- Bina, D., Pelló, R., Richard, J., et al. 2016, *A&A*, 590, A14
- Blanc, G. A., Adams, J. J., Gebhardt, K., et al. 2011, *ApJ*, 736, 31
- Bouwens, R. 2016, in *Astrophys. Space Sci. Lib.*, ed. A. Mesinger, 423, 111
- Bouwens, R. J., Illingworth, G. D., Franx, M., & Ford, H. 2007, *ApJ*, 670, 928
- Bouwens, R. J., Illingworth, G. D., Oesch, P. A., et al. 2015, *ApJ*, 803, 34
- Bouwens, R. J., Smit, R., Labbé, I., et al. 2016, *ApJ*, 831, 176
- Caditz, D. M. 2016, *ApJ*, 831, 50
- Caillier, P., Accardo, M., Adjali, L., et al. 2014, in *Modeling, Systems Engineering, and Project Management for Astronomy VI*, Proc. SPIE, 9150, 91500D
- Casertano, S., de Mello, D., Dickinson, M., et al. 2000, *AJ*, 120, 2747
- Cassata, P., Le Fèvre, O., Garilli, B., et al. 2011, *A&A*, 525, A143
- Conseil, S., Bacon, R., Piqueras, L., & Shepherd, M. 2016, ArXiv e-prints [arXiv:1612.05308]
- Cowie, L. L., & Hu, E. M. 1998, *AJ*, 115, 1319
- Dawson, S., Rhoads, J. E., Malhotra, S., et al. 2007, *ApJ*, 671, 1227
- Dayal, P., & Ferrara, A. 2018, *Phys. Rep.*, 780, 1
- Drake, A. B., Guiderdoni, B., Blaizot, J., et al. 2017a, *MNRAS*, 471, 267
- Drake, A. B., Garel, T., Wisotzki, L., et al. 2017b, *A&A*, 608, A6
- Dunlop, J. S. 2013, in *The First Galaxies*, eds. T. Wiklind, B. Mobasher, & V. Bromm, *Astrophys. Space Sci. Lib.*, 396, 223
- Efron, B., & Petrosian, V. 1992, *ApJ*, 399, 345
- Fan, X., Strauss, M. A., Schneider, D. P., et al. 2001, *AJ*, 121, 54
- Felten, J. E. 1976, *ApJ*, 207, 700
- Furusawa, H., Kosugi, G., Akiyama, M., et al. 2008, *ApJS*, 176, 1
- Giavalisco, M., Ferguson, H. C., Koekemoer, A. M., et al. 2004, *ApJ*, 600, L93
- Grogin, N. A., Kocevski, D. D., Faber, S. M., et al. 2011, *ApJS*, 197, 35
- Gronke, M., Dijkstra, M., Trenti, M., & Wyithe, S. 2015, *MNRAS*, 449, 1284
- Gronwall, C., Ciardullo, R., Hickey, T., et al. 2007, *ApJ*, 667, 79
- Grove, L. F., Fynbo, J. P. U., Ledoux, C., et al. 2009, *A&A*, 497, 689
- Hao, C.-N., Huang, J.-S., Xia, X., et al. 2018, *ApJ*, 864, 145
- Henry, A. L., Martin, C. L., Dressler, A., Sawicki, M., & McCarthy, P. 2012, *ApJ*, 744, 149
- Herenz, E. C., & Wisotzki, L. 2016, *Astrophysics Source Code Library* [record ascl:1612.002]
- Herenz, E. C., & Wisotzki, L. 2017, *A&A*, 602, A111
- Herenz, E. C., Urrutia, T., Wisotzki, L., et al. 2017, *A&A*, 606, A12
- Hill, G. J., Gebhardt, K., Komatsu, E., et al. 2008, in *Panoramic Views of Galaxy Formation and Evolution*, eds. T. Kodama, T. Yamada, & K. Aoki, *ASP Conf. Ser.*, 399, 115
- Hill, G. J., & HETDEX Consortium. 2016, in *Multi-Object Spectroscopy in the Next Decade: Big Questions, Large Surveys, and Wide Fields*, eds. I. Skillen, M. Barcells, & S. Trager, *ASP Conf. Ser.*, 507, 393
- Hogg, D. W. 1999, ArXiv e-prints [arxiv:astro-ph/9905116]
- Hu, E. M., & McMahon, R. G. 1996, *Nature*, 382, 231
- Hu, E. M., Cowie, L. L., & McMahon, R. G. 1998, *ApJ*, 502, L99
- Hu, E. M., Cowie, L. L., Capak, P., et al. 2004, *AJ*, 127, 563
- Hu, E. M., Cowie, L. L., Songaila, A., et al. 2016, *ApJ*, 825, L7
- Hunter, J. D. 2007, *Comput. Sci. Eng.*, 9, 90
- Inami, H., Bacon, R., Brinchmann, J., et al. 2017, *A&A*, 608, A2
- Ivezic, Z., Connelly, A. J., VanderPlas, J. T., & Gray, A. 2014, *Statistics, Data Mining, and Machine Learning in Astronomy* (Princeton, NJ: Princeton University Press)
- James, F. 2006, *Statistical Methods in Experimental Physics*, 2nd edn. (Singapore: World Scientific Publishing Co)
- Johnston, R. 2011, *A&ARv*, 19, 41
- Kerutt, J. 2017, *Astrophysics Source Code Library* [record ascl:1703.011]
- Koekemoer, A. M., Faber, S. M., Ferguson, H. C., et al. 2011, *ApJS*, 197, 36
- Konno, A., Ouchi, M., Nakajima, K., et al. 2016, *ApJ*, 823, 20
- Konno, A., Ouchi, M., Shibuya, T., et al. 2018, *PASJ*, 70, S16
- Kron, R. G. 1980, *ApJS*, 43, 305
- Kudritzki, R.-P., Méndez, R. H., Feldmeier, J. J., et al. 2000, *ApJ*, 536, 19
- Leclercq, F., Bacon, R., Wisotzki, L., et al. 2017, *A&A*, 608, A8
- Le Fèvre, O., Saisse, M., Mancini, D., et al. 2003, in *SPIE Conf. Ser.*, eds. M. Iye, & A. F. M. Moorwood, 4841, 1670
- Lidman, C., Hayes, M., Jones, D. H., et al. 2012, *MNRAS*, 420, 1946
- Luo, B., Brandt, W. N., Xue, Y. Q., et al. 2017, *ApJS*, 228, 2
- Lynden-Bell, D. 1971, *MNRAS*, 155, 95
- Martin, C. L., Sawicki, M., Dressler, A., & McCarthy, P. 2008, *ApJ*, 679, 942
- Mas-Ribas, L., & Dijkstra, M. 2016, *ApJ*, 822, 84
- Matthee, J., Sobral, D., Santos, S., et al. 2015, *MNRAS*, 451, 400
- Matthee, J., Sobral, D., Best, P., et al. 2017, *MNRAS*, 471, 629
- Matthee, J., Sobral, D., Gronke, M., et al. 2018, *A&A*, 619, A136
- Mehta, V., Scarlata, C., Colbert, J. W., et al. 2015, *ApJ*, 811, 141
- Miyazaki, S., Komiyama, Y., Nakaya, H., et al. 2012, in *Ground-based and Airborne Instrumentation for Astronomy IV*, Proc. SPIE, 8446, 84460Z
- Miyazaki, S., Komiyama, Y., Kawamoto, S., et al. 2018, *PASJ*, 70, S1
- Moffat, A. F. J. 1969, *A&A*, 3, 455
- Momose, R., Ouchi, M., Nakajima, K., et al. 2014, *MNRAS*, 442, 110
- Murayama, T., Taniguchi, Y., Scoville, N. Z., et al. 2007, *ApJS*, 172, 523
- Ono, Y., Ouchi, M., Harikane, Y., et al. 2018, *PASJ*, 70, S10
- Ouchi, M., Shimasaku, K., Furusawa, H., et al. 2003, *ApJ*, 582, 60
- Ouchi, M., Shimasaku, K., Akiyama, M., et al. 2008, *ApJS*, 176, 301
- Ouchi, M., Ono, Y., Egami, E., et al. 2009, *ApJ*, 696, 1164
- Ouchi, M., Shimasaku, K., Furusawa, H., et al. 2010, *ApJ*, 723, 869
- Ouchi, M., Harikane, Y., Shibuya, T., et al. 2018, *PASJ*, 70, S13
- Page, M. J., & Carrera, F. J. 2000, *MNRAS*, 311, 433
- Pallottini, A., Ferrara, A., Pacucci, F., et al. 2015, *MNRAS*, 453, 2465
- Partridge, R. B., & Peebles, P. J. E. 1967, *ApJ*, 147, 868
- Peacock, J. A. 1983, *MNRAS*, 202, 615
- Petrosian, V. 1992, in *Luminosity Function of Flux-Limited Samples*, eds. E. D. Feigelson, & G. J. Babu (New York, NY: Springer), 173

- Piqueras, L., Conseil, S., Shepherd, M., et al. 2017, ArXiv e-prints [arXiv:1710.03554]
- Press, W. H., Teukolsky, S. A., Vetterling, W. T., & Flannery, B. P. 1992, *Numerical Recipes in FORTRAN: The Art of Scientific Computing* (Cambridge: Cambridge University Press)
- Pritchett, C. J. 1994, *PASP*, 106, 1052
- Rauch, M., Haehnelt, M., Bunker, A., et al. 2008, *ApJ*, 681, 856
- Sandage, A., Tammann, G. A., & Yahil, A. 1979, *ApJ*, 232, 352
- Santos, S., Sobral, D., & Matthee, J. 2016, *MNRAS*, 463, 1678
- Sawicki, M., Lemaux, B. C., Guhathakurta, P., et al. 2008, *ApJ*, 687, 884
- Schaerer, D., Izotov, Y. I., Verhamme, A., et al. 2016, *A&A*, 591, L8
- Schechter, P. 1976, *ApJ*, 203, 297
- Schmidt, M. 1968, *ApJ*, 151, 393
- Shibuya, T., Ouchi, M., Nakajima, K., et al. 2014, *ApJ*, 788, 74
- Shibuya, T., Ouchi, M., Harikane, Y., et al. 2018a, *PASJ*, 70, S15
- Shibuya, T., Ouchi, M., Konno, A., et al. 2018b, *PASJ*, 70, S14
- Shimasaku, K., Kashikawa, N., Doi, M., et al. 2006, *PASJ*, 58, 313
- Shioya, Y., Taniguchi, Y., Sasaki, S. S., et al. 2009, *ApJ*, 696, 546
- Sobral, D., Matthee, J., Darvish, B., et al. 2015, *ApJ*, 808, 139
- Sobral, D., Santos, S., Matthee, J., et al. 2018a, *MNRAS*, 476, 4725
- Sobral, D., Matthee, J., Darvish, B., et al. 2018b, *MNRAS*, 477, 2817
- Soto, K. T., Lilly, S. J., Bacon, R., Richard, J., & Conseil, S. 2016a, *MNRAS*, 458, 3210
- Soto, K. T., Lilly, S. J., Bacon, R., Richard, J., & Conseil, S. 2016b, Astrophysics Source Code Library [record ascl:1602.003]
- Steidel, C. C., Bogosavljević, M., Shapley, A. E., et al. 2011, *ApJ*, 736, 160
- Steinhardt, C. L., & Jermyn, A. S. 2018, *PASP*, 130, 023001
- Taniguchi, Y., Shioya, Y., Ajiki, M., et al. 2003, *J. Korean Astron. Soc.*, 36, 123
- Tapken, C., Appenzeller, I., Gabasch, A., et al. 2006, *A&A*, 455, 145
- Trujillo, I., Aguerra, J. A. L., Cepa, J., & Gutiérrez, C. M. 2001, *MNRAS*, 328, 977
- van Breukelen, C., Jarvis, M. J., & Venemans, B. P. 2005, *MNRAS*, 359, 895
- Viironen, K., López-Sanjuan, C., Hernández-Monteagudo, C., et al. 2018, *A&A*, 614, A129
- Weilbacher, P. M., Streicher, O., Urrutia, T., et al. 2014, in *Astronomical Data Analysis Software and Systems XXIII*, eds. N. Manset, & P. Forshay, *ASP Conf. Ser.*, 485, 451
- Willmer, C. N. A. 1997, *AJ*, 114, 898
- Wisotzki, L. 1998, *Astron. Nachr.*, 319, 257
- Wisotzki, L., Bacon, R., Blaizot, J., et al. 2016, *A&A*, 587, A98
- Wold, I. G. B., Finkelstein, S. L., Barger, A. J., Cowie, L. L., & Rosenwasser, B. 2017, *ApJ*, 848, 108
- Yuan, Z., & Wang, J. 2013, *Ap&SS*, 345, 305